

# Carbon in different phases ([CII], [CI], and CO) in infrared dark clouds: Cloud formation signatures and carbon gas fractions <sup>★</sup>.

H. Beuther<sup>1</sup>, S.E. Ragan<sup>1</sup>, V. Ossenkopf<sup>2</sup>, S. Glover<sup>3</sup>, Th. Henning<sup>1</sup>, H. Linz<sup>1</sup>, M. Nielbock<sup>1</sup>, O. Krause<sup>1</sup>, J. Stutzki<sup>2</sup>, P. Schilke<sup>2</sup>, and R. Güsten<sup>4</sup>

<sup>1</sup> Max Planck Institute for Astronomy, Königstuhl 17, 69117 Heidelberg, Germany, e-mail: name@mpia.de

<sup>2</sup> I. Physikalisches Institut, University of Cologne, Zùlpicher Strasse 77, 50937 Köln, Germany

<sup>3</sup> Center for Astronomy, Institute for Theoretical Astrophysics, Albert-Überle Strasse 2, 69120 Heidelberg, Germany

<sup>4</sup> Max Planck Institute for Radioastronomy, Auf dem Hügel 69, 53121 Bonn, Germany

Version of January 18, 2021

## ABSTRACT

**Context.** How molecular clouds form out of the atomic phase and what the relative fractions of carbon are in the ionized, atomic, and molecular phase are questions at the heart of cloud and star formation.

**Aims.** We want to understand the kinematic processes of gas flows during the formation of molecular clouds. In addition to that, we aim at determining the abundance ratios of carbon in its various gas phases from the ionized to the molecular form.

**Methods.** Using multiple observatories from Herschel and SOFIA to APEX and the IRAM 30 m telescope, we mapped the ionized and atomic carbon as well as carbon monoxide ([CII] at 1900 GHz, [CI] at 492 GHz, and C<sup>18</sup>O(2–1) at 220 GHz) at high spatial resolution (12'' – 25'') in four young massive infrared dark clouds (IRDCs).

**Results.** The three carbon phases were successfully mapped in all four regions, only in one source does the [CII] line remain a non-detection. With these data, we dissect the spatial and kinematic structure of the four IRDCs and determine the abundances of gas phase carbon in its ionized, atomic, and most abundant molecular form (CO). Both the molecular and atomic phases trace the dense structures well, with [CI] also tracing material at lower column densities. [CII] exhibits diverse morphologies in our sample from compact to diffuse structures, probing the cloud environment. In at least two out of the four regions, we find kinematic signatures strongly indicating that the dense gas filaments have formed out of a dynamically active and turbulent atomic and molecular cloud, potentially from converging gas flows. The atomic carbon-to-CO gas mass ratios are low between 7% and 12% with the lowest values found toward the most quiescent region. In the three regions where [CII] is detected, its mass is always higher by a factor of a few than that of the atomic carbon. While the ionized carbon emission depends on the radiation field, we also find additional signatures that indicate that other processes, for example, energetic gas flows can contribute to the [CII] excitation as well.

**Conclusions.** Combining high-resolution maps in the different carbon phases reveals the dynamic interplay of the various phases of the interstellar medium during cloud formation. Extending these studies to more evolved stages and combining the observations with molecular cloud formation simulations including the chemistry and radiative transfer will significantly improve our understanding of the general interstellar medium, cloud and star formation processes.

**Key words.** Stars: formation – Stars: early-type – Stars: individual: G11.11, G48.66, IRDC 18223, IRDC 18454 – Stars: massive – ISM: clouds – ISM: structure

## 1. Introduction

Carbon is one of the most important species in the interstellar medium (ISM), both in terms of its relevance for the physical and chemical state of the ISM, as well as because of its diagnostic power (e.g., Henning & Salama 1998). Because of its high abundance, carbon is one of the major coolants of the ISM, in its atomic and ionized form for the low-extinction components and in its most abundant molecular form (CO) in high extinction and dense molecular clouds. There are two main pathways linking the sequence C<sup>+</sup>/C<sup>0</sup>/CO: During cloud formation, the originally diffuse and ionized medium recombines and becomes partly neutral (observable in lines of ionized C<sup>+</sup> ([CII]) and neutral carbon C<sup>0</sup> ([CI])), and then with increasing densities forms molecular H<sub>2</sub> and CO (e.g., Bergin et al. 2004; Glover et al. 2010). In con-

trast, if exposed to strong UV radiation, CO can dissociate to form atomic and ionized carbon (e.g., Köster et al. 1994; Röllig et al. 2006).

As atomic hydrogen reacts to form H<sub>2</sub> during cloud formation (e.g., Bergin et al. 2004; Heitsch et al. 2008), the carbon follows the C<sup>+</sup> → C<sup>0</sup> → CO route during the formation of infrared dark clouds (IRDCs). At early evolutionary stages, C<sup>+</sup> is likely to be one of the best tracers for the so-called “dark H<sub>2</sub>” because due to self-shielding H<sub>2</sub> forms earlier than CO (e.g., Langer et al. 2010; Glover & Mac Low 2011). During these processes, signatures of streaming motions may be imprinted on the different carbon lines, allowing us to investigate the cloud formation processes (e.g., Glover et al. 2010; Shetty et al. 2011; Clark et al. 2012).

At the center of IRDCs, massive stars form rapidly, exciting the surrounding gas and producing the different forms of carbon via the opposite CO → C<sup>0</sup> → C<sup>+</sup> route. Photon-dominated region (PDR) models give predictions about the line properties in this scenario (e.g., Tielens & Hollenbach 1985; Cubick

<sup>★</sup> Based on observations carried out with Herschel, Sofia, APEX, and the IRAM 30 m telescope. The data are available in electronic form at the CDS via anonymous ftp to cdsarc.u-strasbg.fr (130.79.128.5) or via <http://cdsweb.u-strasbg.fr/cgi-bin/qcat?J/A+A/>

et al. 2008). Furthermore, the youngest and most embedded protostars develop jets and outflows that form cavities that act as valves releasing UV radiation into the ambient gas (e.g., Kuiper et al. 2010; Cyganowski et al. 2008). Thus, feedback from the youngest protostars affects the relative abundances of molecular CO and atomic and ionized carbon also in the most deeply embedded regions.

Early work has shown that [CII] and [CI] emission is far more extended through molecular clouds than was initially anticipated with layered-structure cloud models. This implied that molecular clouds are clumpy and that the radiation can penetrate the clouds deeply (e.g., Stutzki et al. 1988; Herrmann et al. 1997; Kramer et al. 2004). However, because of the poor spatial resolution available at those times, in particular for  $C^+$ , there was no chance to spatially resolve the substructures, and to disentangle the excitation mechanisms of the different gas components. For example, is the [CII] and [CI] emission deep inside the clouds mainly due to external radiation that penetrates deeply through the clumpy medium, or do internal heating sources from embedded stars contribute significantly to the formation of  $C^+$  and  $C^0$  (e.g., Ossenkopf et al. 2011)? Topics like that can be addressed particularly well for IRDCs because, while they are at early stages of cloud evolution, many already contain internal heating sources that excite the immediate environment (e.g., Rathborne et al. 2006; Beuther et al. 2010; Henning et al. 2010; Wang et al. 2014). This information is also necessary for the proper modeling of the structure and evolution of molecular clouds, since any interior warm gas provides thermal support and deep penetration of UV photons enhances the importance of magnetic support.

To disentangle the different carbon components, it is essential to map the respective regions at high spatial resolution, and to spectrally resolve the line emission. The detailed comparison of the line profiles and their small scale variation between [CII]/[CI]/CO allows us to separate clumps/filaments overlapping along the line of sight. While mapping is important to spatially differentiate the origin of the ionized/atomic/molecular carbon phases, spectral line shape information can be directly compared to cloud formation and PDR model predictions (e.g., Cubick et al. 2008; Glover et al. 2010), as well as to the impact of outflows from the embedded protostars. Mapping at high spectral resolution [CII]/[CI]/CO with Herschel/SOFIA/APEX/IRAM30 m (the Herschel satellite mission, the Stratospheric Observatory For Infrared Astronomy, The Atacama Pathfinder Experiment, and the 30 m telescope of the Institut de Radioastronomie Millimétrique), respectively, can result in spatial resolution elements between  $11''$  and  $15''$ , corresponding to linear scales below 0.2 pc at typical distances of IRDCs of 3 kpc. This matches the physical processes of cloud formation, fragmentation and feedback extremely well, e.g., the Jeans fragmentation scale at typical densities ( $\sim 10^3 \text{ cm}^{-3}$ ) is on that order.

To address these aspects, we conducted a concerted effort to study the gas phase carbon budget in young molecular clouds by observing and analyzing a well selected sample of four IRDCs in [CII] at  $158 \mu\text{m}$  with Herschel and SOFIA, in [CI] with APEX and in  $^{13}\text{CO}/\text{C}^{18}\text{O}(2-1)$  with the IRAM 30 m telescope. This combined mapping approach is complementary to the GOTC<sup>+</sup> Herschel key project (Galactic Observations of Terahertz  $C^+$ , Langer et al. 2010; Pineda et al. 2013) that focused on single pointings toward a large sample of Galactic sources. Now mapping the regions allows us to separate the different cloud components and their associated carbon constituents properly from low to high extinction. These data provide us with the column densities, the spatial structure and the kinematic/dynamic

properties of the different states of carbon in the ISM. For all regions we have complementary PACS/SPIRE continuum data (EPOS Herschel GT project, Ragan et al. 2012) as well as APEX/LABOCA  $870 \mu\text{m}$  continuum observations (Schuller et al., 2009).

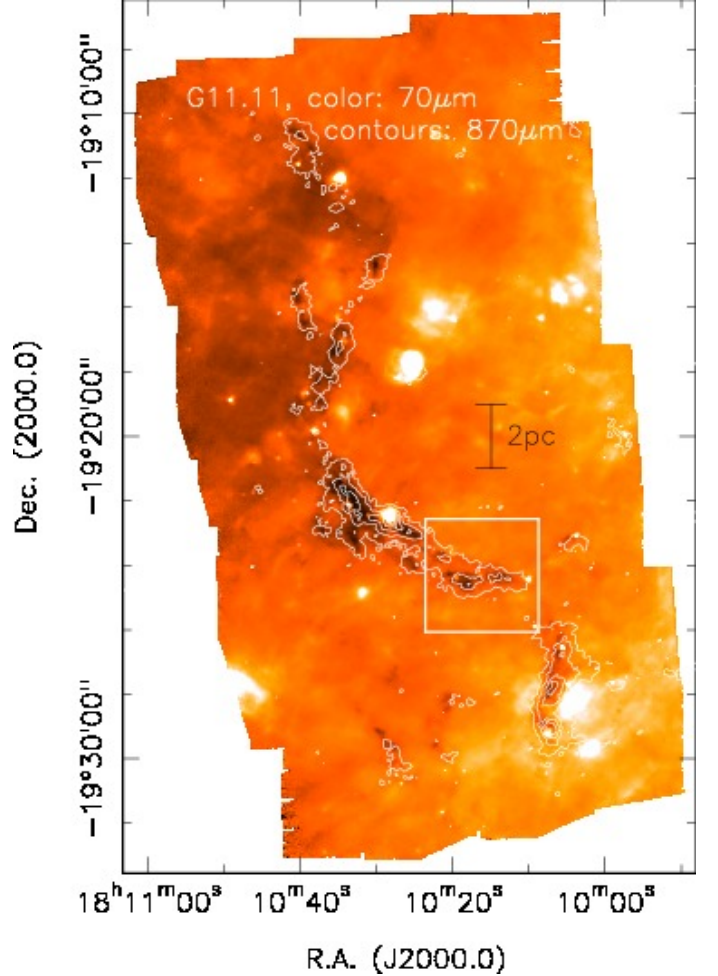


**Fig. 1.** G11.11: Large-scale Herschel/PACS  $70 \mu\text{m}$  image of the G11.11 region with  $870 \mu\text{m}$  ATLASGAL contours starting at 200 and continuing in  $300 \text{ mJy beam}^{-1}$  steps (Henning et al., 2010). The white box outlines the region of our carbon observations shown in Fig. 2.

## 2. The Sample

We selected four infrared dark clouds that exhibit a variety of environments. While G11.11 (also known as The Snake, e.g., Henning et al. 2010; Kainulainen et al. 2013) and G48.66 (e.g., Ossenkopf et al. 2011; Pitann et al. 2013) are rather isolated IRDCs (G48.66 shows slightly more star formation activity), IRDC 18223 is an infrared dark filament that has already formed a high-mass protostellar object with  $\sim 10^4 L_\odot$  at one end (e.g., Beuther et al. 2010). Finally, IRDC 18454 is also a starless dark cloud, however in the very close environment of the Galactic mini-starburst W43 (Beuther et al., 2013). All these clouds are part of the Herschel key project EPOS with a wealth of complementary data (Ragan et al., 2012). Table 1 presents the basic sample parameters.

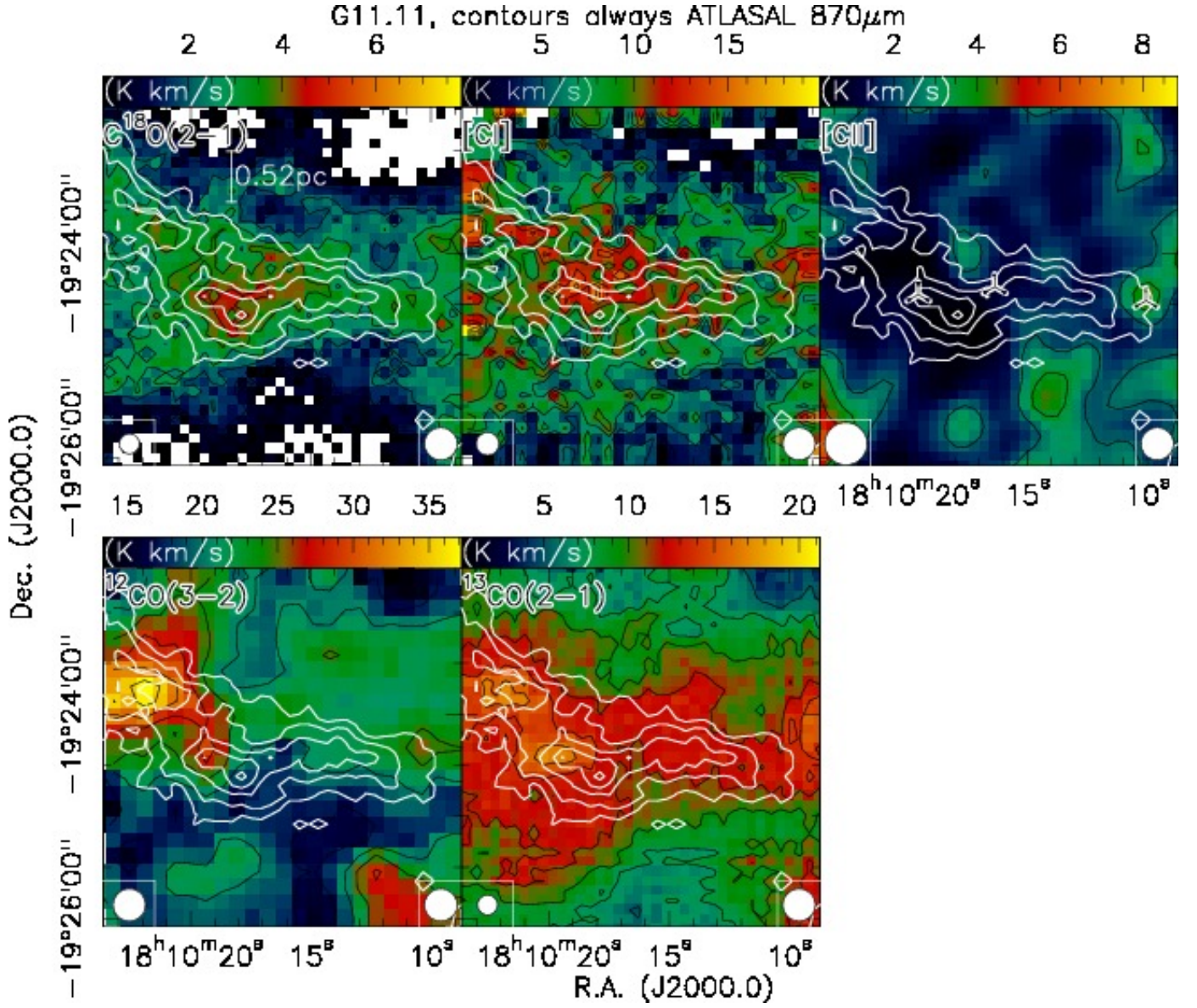


**Fig. 2.** G11.11: The color scale shows integrated intensity images of the transitions marked above each panel. Integration regimes are  $[27,33]$   $\text{km s}^{-1}$ ,  $[27,33]$   $\text{km s}^{-1}$ ,  $[29,31]$   $\text{km s}^{-1}$ ,  $[24,38]$   $\text{km s}^{-1}$  and  $[24,36]$   $\text{km s}^{-1}$  for  $\text{C}^{18}\text{O}(2-1)$ ,  $[\text{C I}]$ ,  $[\text{C II}]$ ,  $^{12}\text{CO}(3-2)$  and  $^{13}\text{CO}(2-1)$ , respectively. Except for  $[\text{C II}]$ , the corresponding black contours start from 15% and continue in 10% steps of the peak emission in each map. The peak values are 7.8, 19.9, 37.1 and 21.2  $\text{K km s}^{-1}$ , respectively. The  $[\text{C II}]$  contours start at  $3\sigma$  and continue in  $1\sigma$  steps of  $0.8 \text{ K km s}^{-1}$ . The white contours always show the ATLASGAL  $870 \mu\text{m}$  continuum image starting at a  $3\sigma$  level of  $0.15 \text{ Jy beam}^{-1}$  and continue in  $4\sigma$  steps. The bottom-left of each panel shows the beam of the line data whereas the bottom-right shows the continuum beam size. The three markers in the  $[\text{C II}]$  panel show the positions of  $70 \mu\text{m}$  sources, and the top-left panel also shows a linear scale-bar.

**Table 1.** The Sample

| Name      | R.A.<br>(J2000.0) | Dec.<br>(J2000.0) | D<br>(kpc)       | $v_{\text{lsr}}$<br>( $\text{km s}^{-1}$ ) |
|-----------|-------------------|-------------------|------------------|--------------------------------------------|
| G11.11    | 18:10:16.00       | -19:24:22.0       | 3.4              | 29.2                                       |
| G48.66    | 19:21:48.00       | 13:49:06.0        | 2.6              | 34.0                                       |
| IRDC18223 | 18:25:08.46       | -12:45:05.0       | 3.5              | 45.5                                       |
| IRDC18454 | 18:47:59.20       | -01:54:05.0       | 5.5 <sup>1</sup> | 52.8/100.2 <sup>2</sup>                    |

Most distances and  $v_{\text{lsr}}$  are taken from Ragan et al. (2012).

<sup>1</sup> Zhang et al. (2014), <sup>2</sup> Beuther & Sridharan (2007)

**Table 2.** Observed spectral lines

| Freq.<br>(GHz) | Transitions                            | $E_u/k$<br>(K) |
|----------------|----------------------------------------|----------------|
| 1900.5372      | $[\text{C II}](^2P_{3/2} - ^2P_{1/2})$ | 91.2           |
| 492.1607       | $[\text{C I}](^3P_1 - ^3P_0)$          | 23.6           |
| 219.5603       | $\text{C}^{18}\text{O}(2-1)$           | 15.8           |
| 220.3987       | $^{13}\text{CO}(2-1)$                  | 15.9           |
| 345.7960       | $^{12}\text{CO}(3-2)$                  | 33.2           |

### 3. Observations

The different spectral lines shown in Table 2 were observed with various instruments, the ionized carbon  $[\text{C II}]$  line with

Herschel/HIFI (Pilbratt et al. 2010; de Graauw et al. 2010, for G11.11, G48.66, IRDC18454) and SOFIA/GREAT (Young et al. 2012; Heyminck et al. 2012, for IRDC 18223), the atomic carbon  $[\text{C I}](^3P_1 - ^3P_0)$  and  $^{12}\text{CO}(3-2)$  with APEX, and the  $\text{C}^{18}\text{O}(2-1)$



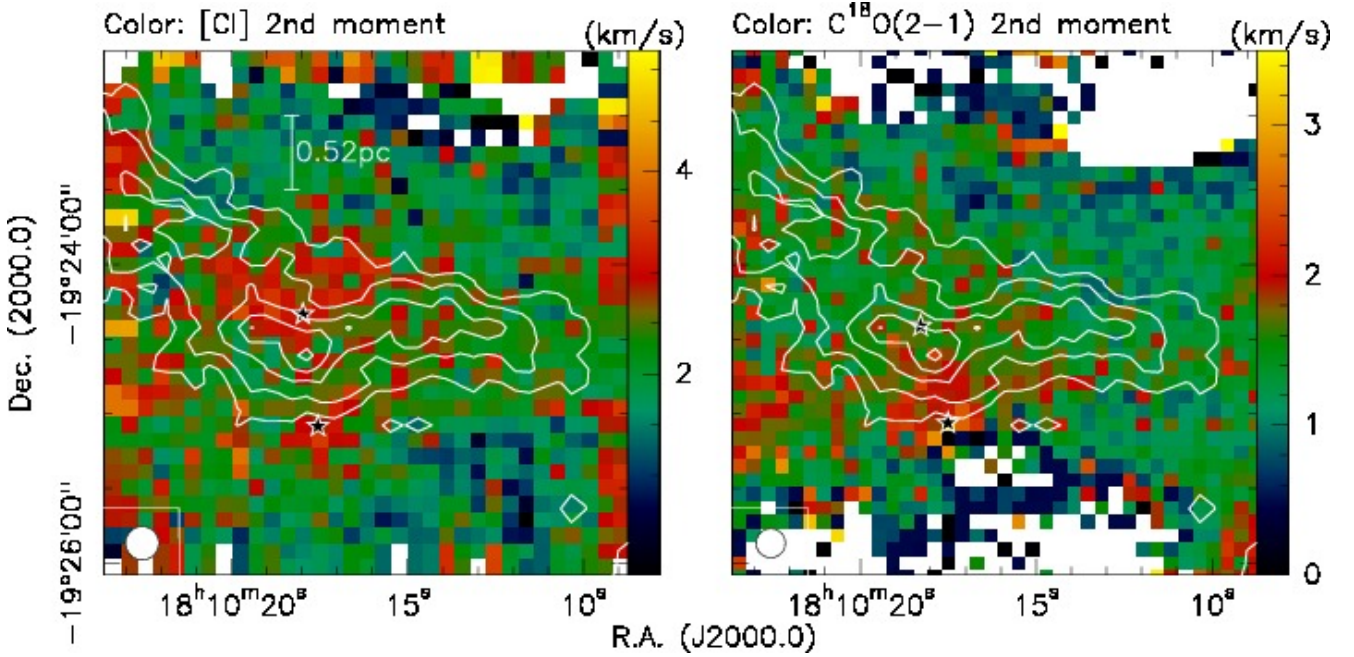


**Fig. 4.** G11.11: The color scales show the 2nd moment maps (intensity weighted line widths) of [CI] and  $\text{C}^{18}\text{O}(2-1)$  in the left and right panel, respectively. The contours present the ATLASGAL  $870\,\mu\text{m}$  emission with the same contours as in Fig. 2. The bottom-left of each panel shows the beam of the line data, and the left panel also presents a linear scale-bar. The five-pointed stars mark the positions toward which the spectra in Fig. 5 are extracted.

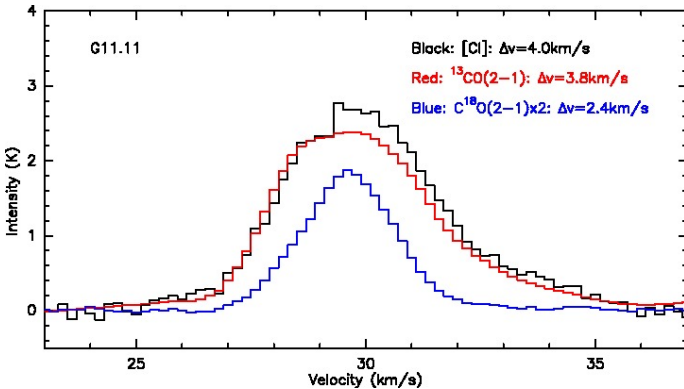


**Fig. 3.** G11.11:  $\text{C}^{18}\text{O}(2-1)$ ,  $^{13}\text{CO}(2-1)$  and [CI] spectra averaged over the whole area of emission shown in Figure 2.

and  $^{13}\text{CO}(2-1)$  with the IRAM 30 m telescope. All data are calibrated to  $T_{\text{mb}}$  in Kelvin. The final spectral resolution  $\Delta\nu$ , the  $1\sigma$  rms in a line-free channel and the spatial resolution  $\theta$  for all data can be found in Table 3.

The Herschel/HIFI [CII] data for G11.11, G48.66 and IRDC18454 were observed in one guaranteed time (obsids 1342250966, 1342250967) and one open time project (obsids 1342270620, 1342270621, 1342270624, 1342270625). The approximate map sizes were in all cases  $\sim 3' \times 3'$ , and each map was observed twice at scanning angles of 0 and 90 deg. Data reduction was conducted within HIPE version 10.3 and beam and forward efficiencies of 0.69 and 0.96 were applied (Roelfsema et al., 2012). The observations were taken against the internal cold load as reference and included the observation of an additional OFF position at an offset of R.A.  $+5'$  and Dec.  $-5'$  from the center of the map. As we found clear contamination of the OFF position, we only subtracted the load reference from the data, and removed the remaining standing wave pattern by the

HifiFitFringe pipeline task which resulted in good baselines for our spectra. The spectra were then exported to GILDAS format for final processing and imaging. For G11.11 we used only the V-polarization because that had less standing wave problems. For the other two sources, we used both polarizations. To increase the signal-to-noise ratio, we degraded the native spatial resolution of  $\sim 12''$  to  $20'' - 25''$  (Table 3).

The corresponding [CII] data for IRDC 18223 were observed in fall 2013 with GREAT on SOFIA and a beam efficiency of 0.67 (Heyminck et al., 2012). These data were smoothed to  $20''$  resolution to increase the signal-to-noise ratio as well.

The atomic carbon [CI] data were all obtained with the APEX observatory and the FLASH receiver. The maps have similar sizes as the [CII] maps and were observed in on-the-fly mode at a spatial resolution of  $\sim 13.5''$  and a native spectral resolution of  $0.05\,\text{km s}^{-1}$ . We re-binned the spectra to improve the signal to noise, and the finally used effective spectral resolution  $\Delta\nu$ ,  $1\sigma$  and  $\theta$  can be found in Table 3. The FLASH receiver observed simultaneously the  $^{12}\text{CO}(3-2)$  line, but we show that only for G11.11 as an example because our analysis relies on the  $\text{C}^{18}\text{O}(2-1)$  data due to its lower optical depth.

Finally, the  $\text{C}^{18}\text{O}(2-1)$  spectra were all observed during different runs with the IRAM 30 m telescope. The maps were taken in the on-the-fly mode, and the spatial resolution is  $\sim 12''$ . The data for G11.11, G48.66 and IRDC 18223 were observed as pooled observations in winter 2012. The observations for IRDC 18454 were part of an IRAM large program (PI F. Motte) and have already been published in Carlhoff et al. (2013). The IRAM 30 m telescope also observed simultaneously the  $^{13}\text{CO}(2-1)$  line, but we again only show it for G11.11 as an example and rely for the analysis on the  $\text{C}^{18}\text{O}(2-1)$  data. The corresponding  $870\,\mu\text{m}$  continuum data were taken from the ATLASGAL survey (Schuller et al., 2009).

**Table 3.** Observing parameters

| Source    | $\Delta v$             | $1\sigma$ | $\theta$ | $\Delta v$ | $1\sigma$ | $\theta$ | $\Delta v$         | $1\sigma$ | $\theta$ |
|-----------|------------------------|-----------|----------|------------|-----------|----------|--------------------|-----------|----------|
|           | (km s <sup>-1</sup> )  | (K)       | ( $''$ ) |            | (K)       | ( $''$ ) |                    | (K)       | ( $''$ ) |
|           | C <sup>18</sup> O(2–1) |           |          | [CI]       |           |          | [CII] <sup>1</sup> |           |          |
| G11.11    | 0.4                    | 0.16      | 12       | 0.4        | 0.6       | 13.5     | 0.08               | 0.32      | 25       |
| G48.66    | 0.27                   | 0.25      | 12       | 0.2        | 1.0       | 13.5     | 0.08               | 0.31      | 20       |
| IRDC18223 | 0.27                   | 0.2       | 12       | 0.3        | 0.6       | 13.5     | 0.2                | 0.28      | 20       |
| IRDC18454 | 1.5                    | 0.13      | 12       | 0.2        | 0.9       | 13.5     | 0.08               | 0.38      | 20       |

$\Delta v$ ,  $1\sigma$  and  $\theta$  are the spectral resolution,  $1\sigma$  rms and beam size, respectively, for the three transitions.

<sup>1</sup> The [CII] data from G11.11, G48.66 and IRDC 18454 are from Herschel, the [CII] data for IRDC 18223 are from SOFIA.

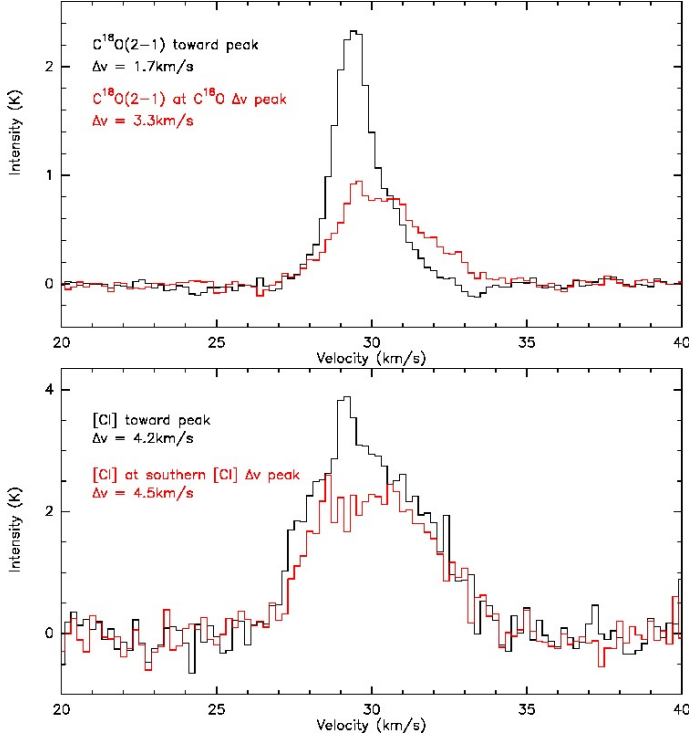


**Fig. 5.** G11.11: C<sup>18</sup>O(2–1) (top-panel) and [CI] spectra (bottom panel) at selected positions as marked in the panel and in Figure 4.

## 4. Results

### 4.1. Morphologies and structures

Since our data are the first maps in the different gas carbon phases, we start with a morphological and structural analysis of the data toward the four IRDCs.

#### 4.1.1. G11.11 also known as The Snake:

The IRDC G11.11 encompasses a much larger area than shown in Fig. 1. Here we focus on the  $3' \times 3'$  region outlined by the white box. That subregion is a particularly quiescent part of the G11.11 region, hosting only very few weak mid-infrared sources as well as a dark core without any mid- or far-infrared counterpart (Henning et al., 2010; Ragan et al., 2012). Figure 2 presents the different carbon datasets we obtained for this project. The  $870\mu\text{m}$  submm continuum data tracing the cold dust emission are shown in contours as reference frame on all plots. The first and most obvious outcome for G11.11 is that the molecular C<sup>18</sup>O and atomic carbon emission do trace the high-column density gas probed by the  $870\mu\text{m}$  continuum emission well. While

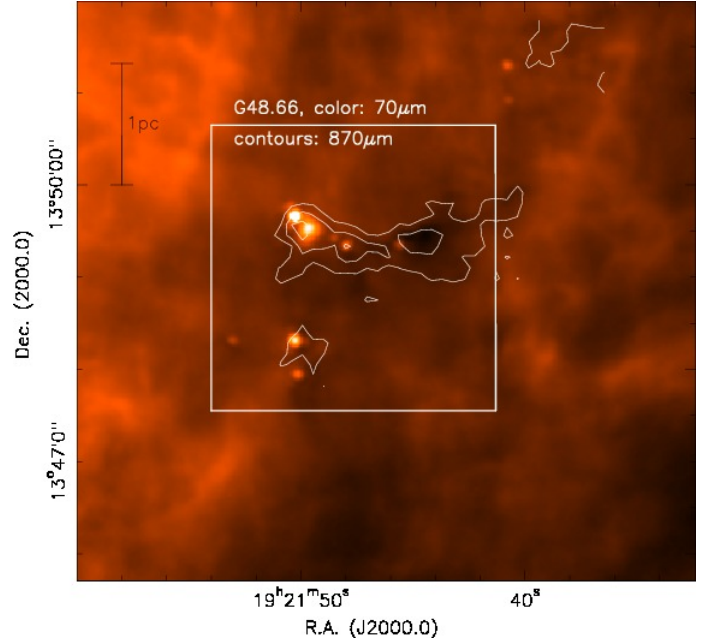


**Fig. 6.** G48.66: Large-scale Herschel/PACS  $70\mu\text{m}$  image of the G48.66 region with  $870\mu\text{m}$  ATLASGAL contours in  $3\sigma$  steps of  $150\text{ mJy beam}^{-1}$ . The white box outlines the region of our carbon observations shown in Fig. 7 (Pitann et al., 2013).

the C<sup>18</sup>O(2–1) emission follows closely the dust continuum, the atomic [CI] emission appears a bit more extended. In contrast to these two tracers, the ionized carbon [CII] emission remains a non-detection in our data. Towards the dust continuum, we do not detect any [CII] at all, but a few very weak features are tentatively identified at the cloud edges. However, none of these integrated emission edge features are above  $6\sigma$ , and analyzing individual spectra at these position, we cannot confirm them either. Hence, at the given sensitivity, our [CII] observations toward G11.11 are a non-detection, even after averaging all spectra over the entire region.

Figure 2 also shows the  $^{12}\text{CO}(3-2)$  emission from APEX and the  $^{13}\text{CO}(2-1)$  emission from the IRAM30 m telescope. However, both trace the dense gas emission outlined by the dust continuum worse than the C<sup>18</sup>O(2–1). This is mainly due to the larger optical depth of these isotopologues. For the remainder of the analysis, we therefore focus on the C<sup>18</sup>O(2–1) data because of its low optical depth.

Figure 3 presents the averaged spectra over the entire region of emission in Figure 2 for C<sup>18</sup>O(2–1),  $^{13}\text{CO}(2-1)$  and [CI]. While the line shape does vary significantly between the different species, the line width measured as full width half maximum is similar for [CI] and  $^{13}\text{CO}(2-1)$  ( $\Delta v = 4.0$  and



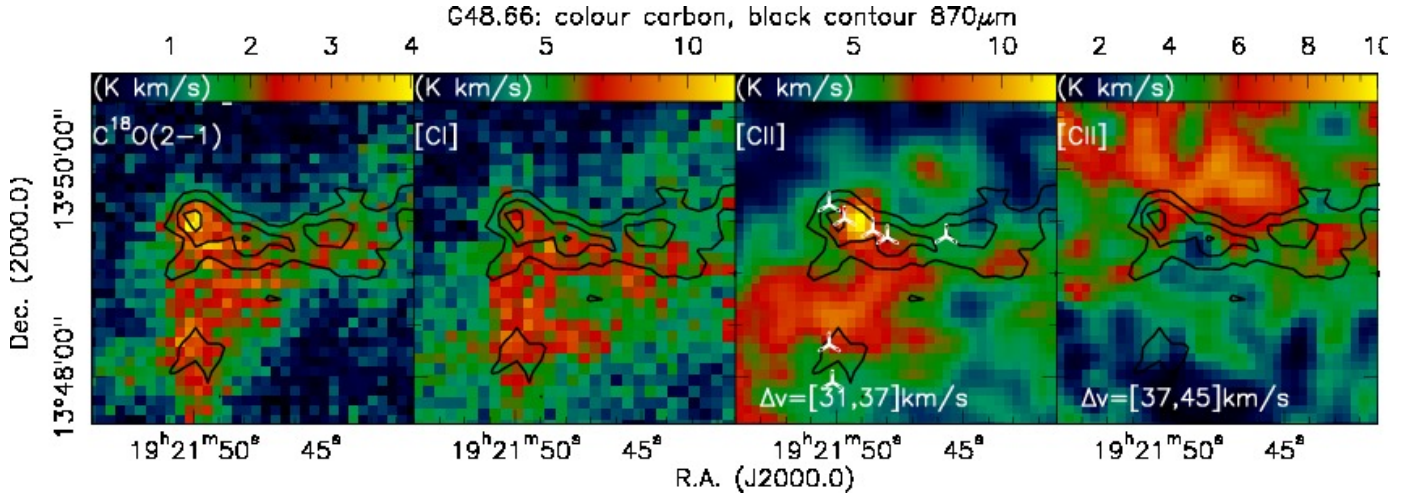


**Fig. 7.** G48.66: The color scale shows from left to right the emission from  $C^{18}O(2-1)$ , [CI] and [CII], respectively. The integration ranges for  $C^{18}O(2-1)$  and [CI] are  $[32.0; 35.0]$  and  $[32.0; 35.5]$   $\text{km s}^{-1}$ . The integration ranges for [CII] are marked in the 2 right panels. The contours always show the ATLASGAL  $870 \mu\text{m}$  emission starting at  $3\sigma$  level of  $150 \text{ mJy beam}^{-1}$  and continuing in  $3\sigma$  steps. The white markers in the 3rd panel mark the positions of  $70 \mu\text{m}$  sources.

$3.8 \text{ km s}^{-1}$ , respectively), whereas it is narrower for  $C^{18}O(2-1)$  ( $\Delta v = 2.4 \text{ km s}^{-1}$ ). Since  $^{13}\text{CO}$  and [CI] trace larger volumes than  $C^{18}O$ , this difference is approximately consistent with Larson’s line width-size relation (Larson, 1981; Stahler & Palla, 2005). Although the averaged line width over the whole cloud of [CI] and  $^{13}\text{CO}(2-1)$  are similar, their spatial structure varies considerably.

For a closer comparison of the  $C^{18}O(2-1)$  and [CI] line width distribution, Figure 4 presents 2nd moment maps (intensity-weighted line widths) of both lines. Interestingly, the [CI] line width peaks close to the main submm continuum sources and hence resembles the [CI] integrated intensity image in Figure 2. Together with the non-Gaussian profiles, this is consistent with a macro-turbulent picture, where individual, partially optically thick clumps are distributed over some turbulent velocity interval. In contrast to that, the  $C^{18}O(2-1)$  2nd moment map shows a relatively smooth velocity distribution over most of the clump with only an increase in line width south of the main submm continuum peak. The same position shows also an increased line width in the [CI] emission. Figure 5 present the  $C^{18}O(2-1)$  and [CI] spectra extracted toward the respective integrated intensity as well as line width peak positions, and the same trend is visible there. While the [CI] line widths between both positions does not vary much, for  $C^{18}O(2-1)$  we find a unique line width increase toward that southern position at the edge of cloud. Interestingly, Ragan et al. (in prep.) find toward the close-by submm continuum peak position (Fig. 4) multiple  $\text{N}_2\text{H}^+$  velocity components in high-spatial-resolution Plateau de Bure Interferometer (PdBI) data. These multiple  $\text{N}_2\text{H}^+$  spectral features are consistent with global collapse of massive gas clumps as modeled by Smith et al. (2013). Although the positions of our enhanced  $C^{18}O$  and [CI] line width do not exactly coincide with the multiple  $\text{N}_2\text{H}^+$  spectra (offset  $\sim 25''$ ), the close spatial association may indicate that both features could trace different parts of the same global collapse of this star-forming region.

#### 4.1.2. G48.66:

The IRDC G48.66 is a prominent massive dark cloud in the projected vicinity of W51 (distance  $\sim 5.4 \text{ kpc}$ , Sato et al. 2010), however at closer distance of  $2.6 \text{ kpc}$  (e.g., Ormel et al. 2005; van

der Wiel & Shipman 2008). A recent analysis of the Herschel far-infrared continuum data of that IRDC has been published by Pitann et al. (2013). Figure 6 shows the  $70 \mu\text{m}$  Herschel/PACS image outlining the dark features but also several embedded protostars within the cloud (the area of our carbon spectral line observations is marked). Compared to the region within G11.11 discussed in the previous section, G48.66 appears slightly more evolved, yet still very young.

The integrated emission maps of the different carbon phases of this region are presented in Figure 7. In G48.66 the  $C^{18}O(2-1)$  and [CI] emission follows the dense gas in east-west direction traced by the ATLASGAL  $870 \mu\text{m}$  emission, and it exhibits an additional extension toward the south of that east-west ridge. The [CI] map exhibits even larger differences with more emission in east-west extension in the southern part of the map. These spatial substructures could not be identified by the previous lower-spatial-resolution [CI] observations by Ossenkopf et al. (2011) but are consistent with the two peaks of emission seen there.

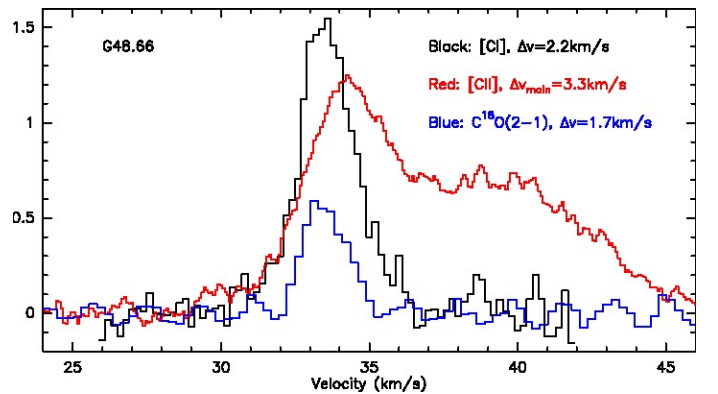


**Fig. 8.** G48.66:  $C^{18}O(2-1)$ , [CI] and [CII] spectra (in K) averaged over the whole area of emission shown in Figure 7. The FWHM of the main peak at  $34 \text{ km s}^{-1}$  are presented as well.

The biggest difference arises in the ionized carbon [CII] map. In contrast to G11.11, where we barely detect the line above the  $3\sigma$  level, here [CII] is strong and shows even different velocity components. While  $C^{18}O(2-1)$  and [CI] have single-peaked

spectra around the  $v_{lsr}$  of  $\sim 34 \text{ km s}^{-1}$  with averaged full-width-half-maximum (FWHM) values of  $1.7$  and  $2.2 \text{ km s}^{-1}$ , respectively (Fig. 8), the [CII] spectrum exhibits a very broad second component extending up to  $45 \text{ km s}^{-1}$  (Fig. 8, the FWHM of the main component at  $\sim 34 \text{ km s}^{-1}$  is  $3.3 \text{ km s}^{-1}$ ). Analyzing the spatial structure of these two velocity components, we find that the one around the  $v_{lsr}$  is similar to the [CI] emission. Although the [CII] peak position is a bit offset from the  $\text{C}^{18}\text{O}$  and dust continuum peak, the large-scale structure of that component resembles that of the [CI] and  $\text{C}^{18}\text{O}$  emission. In contrast to that, the high-velocity component is distinctively shifted to the north (the right two panels in Figure 7). A different way to dissect the velocity structure of the ionized carbon emission is a 1st moment map (intensity-weighted peak velocity). The velocity pattern shown in Figure 9 is dominated by a steep velocity gradient right across the dense cloud filament seen in the submm dust continuum emission as well as the infrared extinction. We will discuss that gradient in more detail in section 5.2.

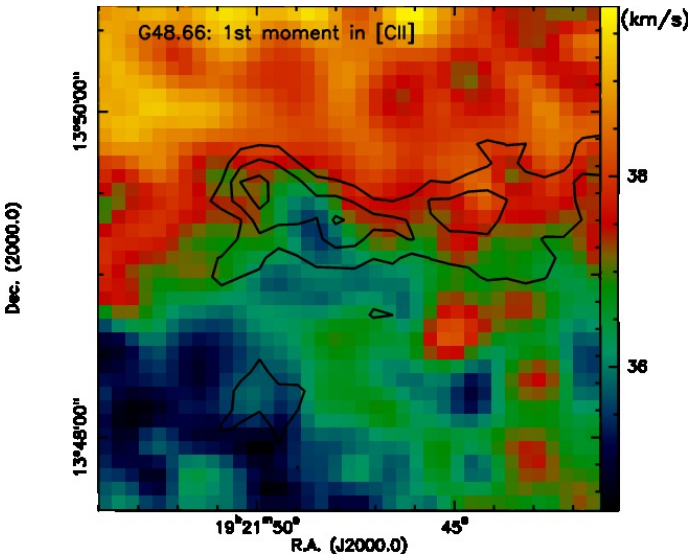


**Fig. 9.** G48.66: The color scale presents the 1st moment (intensity-weighted velocity) of the [CII] emission between  $30$  and  $45 \text{ km s}^{-1}$ . The contours show the ATLASGAL  $870 \mu\text{m}$  emission starting at  $3\sigma$  level of  $150 \text{ mJy beam}^{-1}$  and continuing in  $3\sigma$  steps.

#### 4.1.3. IRDC 18223:

The IRDC 18223 has been studied in detail in recent years on scales of the filament (e.g., Beuther et al. 2002, 2010; Garay et al. 2004) as well as on smaller scales of individual substructures (e.g., Beuther & Steinacker 2007; Fallscheer et al. 2009). This filamentary IRDC hosts several evolutionary stages from an already evolved high-mass protostellar object (HMPO) in the north to the dark filament with embedded very young protostars (Fig. 10). It is also part of a much larger filament extending more than  $70 \text{ pc}$  in the Milky Way plane (e.g., Tackenberg et al. 2013; Ragan et al. 2014). For this carbon study we focus in particular on the infrared dark filament outlined in Figure 10.

The spatial and spectral structure of the molecular  $\text{C}^{18}\text{O}$ , atomic and ionized carbon in this region are presented in Figures 11 and 12. Around the  $v_{lsr}$  of  $\sim 45.5 \text{ km s}^{-1}$ , the main emission is seen in the molecular  $\text{C}^{18}\text{O}(2-1)$  and the atomic [CI] emission, and both species exhibit a secondary strong peak around  $51 \text{ km s}^{-1}$ . The averaged spectrum over the whole region in the

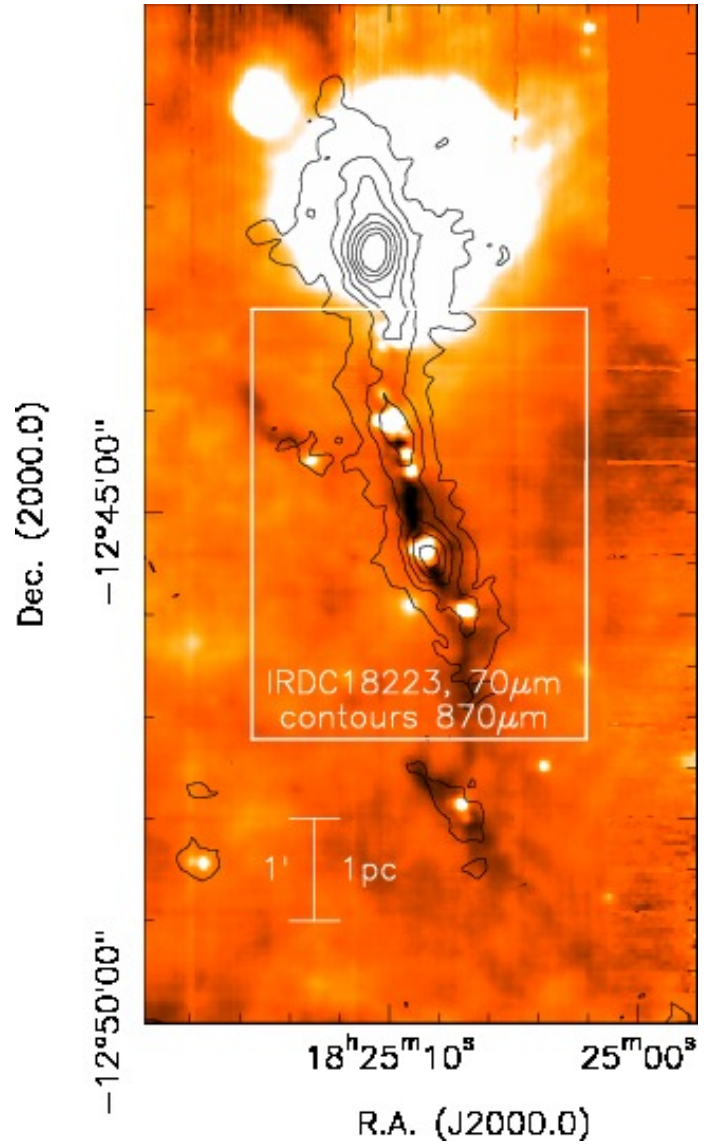


**Fig. 10.** IRDC 18223: Large-scale Herschel/PACS  $70 \mu\text{m}$  image of the IRDC 18223 region with  $870 \mu\text{m}$  ATLASGAL contours starting at  $200$  and continuing in  $300 \text{ mJy beam}^{-1}$  steps. The white box outlines the region of our carbon observations shown in Fig. 11.

ionized [CII] line shows emission peaks at similar velocities, however, the intensities of both peaks are almost the same. All three species exhibit a third spectral peak at slightly higher velocities of  $\sim 54.5 \text{ km s}^{-1}$ . The [CI] spectrum in Figure 12 exhibits an additional weak emission component between approximately  $35$  and  $41 \text{ km s}^{-1}$ . However, the images show that this component is only found at the south-eastern edge of our map and barely covered at all. Therefore, we do not show it here.

Figure 13 shows the spatial structure of these three velocity components for the atomic [CI] line. The main spectral component between  $42$  and  $49 \text{ km s}^{-1}$  is strongly correlated with the dense gas traced by the  $1.2 \text{ mm}$  dust continuum emission measured with MAMBO at the IRAM  $30 \text{ m}$  telescope (Beuther et al., 2002). However, already the high-velocity end of this component between  $46.8$  and  $48 \text{ km s}^{-1}$  exhibits a spatially distinct structure visible in the cyan contours in Figure 13 (left panel). In contrast to this, the second component between  $49$  and  $53 \text{ km s}^{-1}$  which is also strong in the averaged spectrum (Fig. 12) appears spatially diffuse with barely any obvious peak emission (Fig. 13



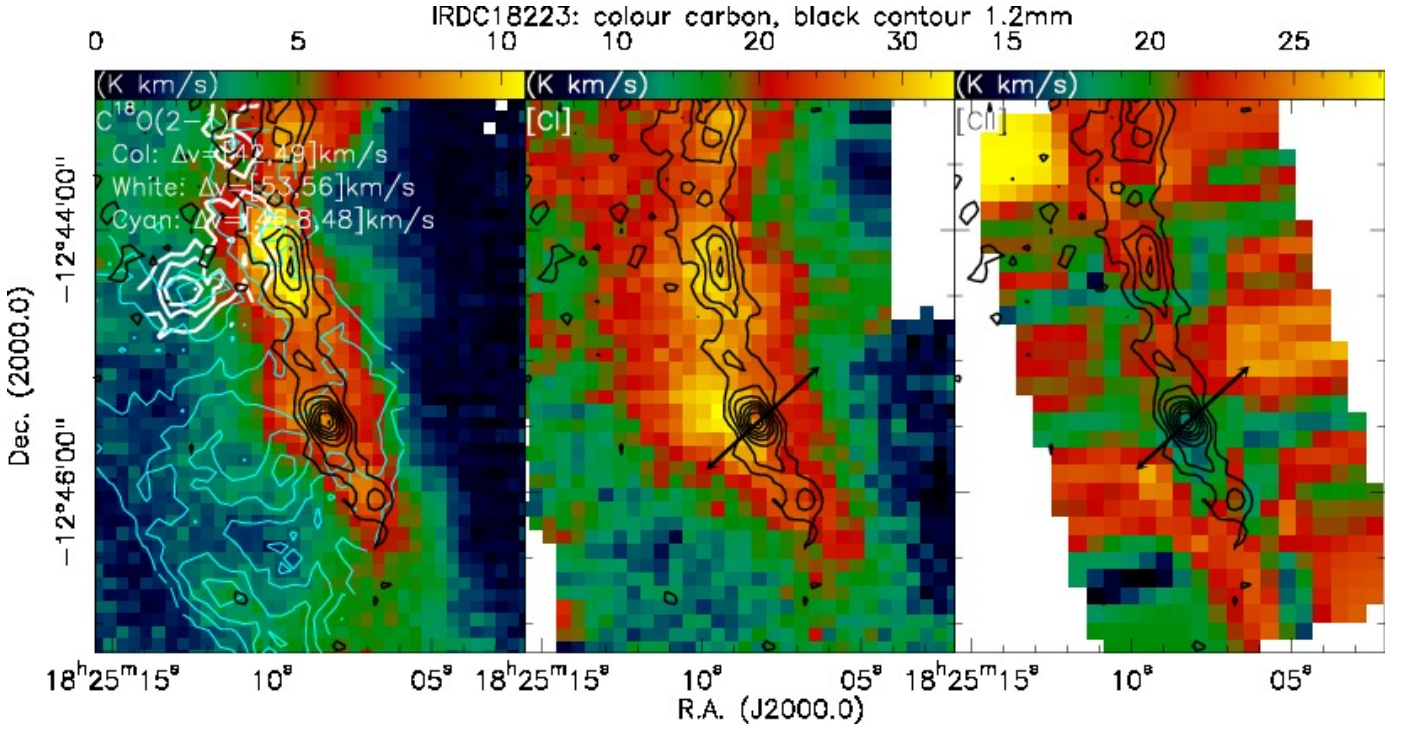


**Fig. 11.** IRDC18223: The color scale shows in the left, middle and right panel the emission from  $\text{C}^{18}\text{O}(2-1)$ , [CI] and [CII], respectively. The integration regimes for the three color images are [42;49], [43;49] and [43;55]  $\text{km s}^{-1}$ . The white and cyan contours in the left panel correspond to the velocity components at [53.0;56.0] and [46.9;48.0]  $\text{km s}^{-1}$ . The black contours always show the 1.2 mm continuum emission (Beuther et al., 2002) starting at  $3\sigma$  level of  $36 \text{ mJy beam}^{-1}$  and continuing in  $3\sigma$  steps. The arrows in the middle and right panel outline the direction of a bipolar outflow studied by Fallscheer et al. (2009).

middle panel). Going to even higher velocities the spectral component between 53 and 56  $\text{km s}^{-1}$  is spatially very localized with a small peak to the east of the filament (Fig. 13 right panel and Fig. 11 left panel). The spatial structure of the  $\text{C}^{18}\text{O}(2-1)$  emission is similar to the [CI] line, whereas for the [CII] emission we do not find clear structures, but the ionized carbon appears to be distributed much more diffusely over the entire complex without any clear association with the infrared dark filament. Interestingly, two strong [CII] emission features lie southeast and northwest of the central peak in the filament in the direction of the two outflow lobes discussed in Fallscheer et al. (2009). While this is not conclusive, there is the possibility that these [CII] emission features could be partly related to the outflow from the embedded young protostar.

#### 4.1.4. IRDC 18454:

The fourth region in our sample, IRDC 18454, is in the direct vicinity of the Galactic mini-starburst W43. Figure 14 presents the  $70 \mu\text{m}$  emission of the region, and while W43 at the western edge is very bright in the far-infrared, our regions of interest are either faint at  $70 \mu\text{m}$  or they even show dark absorption patches.

Another intriguing aspect of this region at the interface of the Galactic bar with the inner spiral arm, is the velocity structure. Toward this region, all observed spectral lines exhibit 2 spectral components, one centered at approximately  $100 \text{ km s}^{-1}$  and the second at  $\sim 50 \text{ km s}^{-1}$  (Figure 16). This is not just observed in the carbon tracers shown here, but also in dense gas tracers like  $\text{N}_2\text{H}^+$  or  $\text{NH}_3$  (e.g., Nguyen Luong et al. 2011; Beuther et al. 2012). Also Galactic surveys of radio recombination lines show a large fraction of multiple components in this part of the Galaxy (Anderson et al., 2011). These different components could be

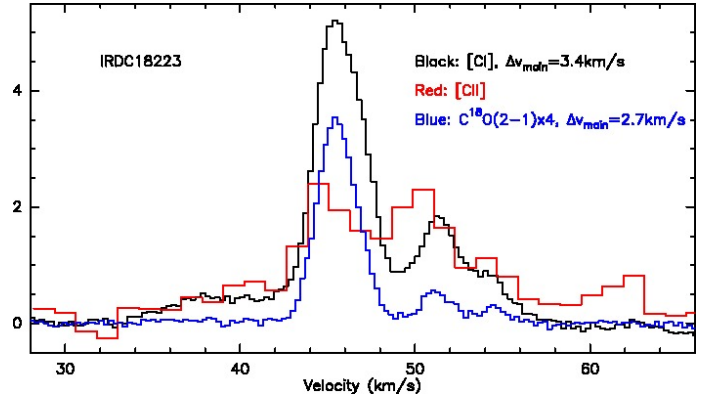


**Fig. 12.** IRDC18223:  $\text{C}^{18}\text{O}(2-1)$ , [CI] and [CII] spectra (in K) averaged over the whole area of emission shown in Figure 11. The fitted [CI] and  $\text{C}^{18}\text{O}(2-1)$  FWHM of the main component around  $45 \text{ km s}^{-1}$  are presented as well (class did not converge to a reasonable fit result for the [CII] line).

caused by two independent clouds in different spiral arms (e.g., Nguyen Luong et al. 2011), via colliding gas flows (e.g., Carlhoff et al. 2013), or by potential cloud-cloud interaction in the interface between the Galactic bar and the inner Scutum spiral arm (e.g., Beuther et al. 2012). For a detailed discussion about this IRDC, the influence of the neighboring W43 mini-starburst and the multiple velocity components see Beuther et al. (2012).

Independent of the interpretation of the different velocity components, the velocity spread of each individual component is very broad, for the high-velocity component it ranges from approximately  $65$  to  $140 \text{ km s}^{-1}$ , and these velocities are all spatially connected (Nguyen Luong et al., 2011). Because of the



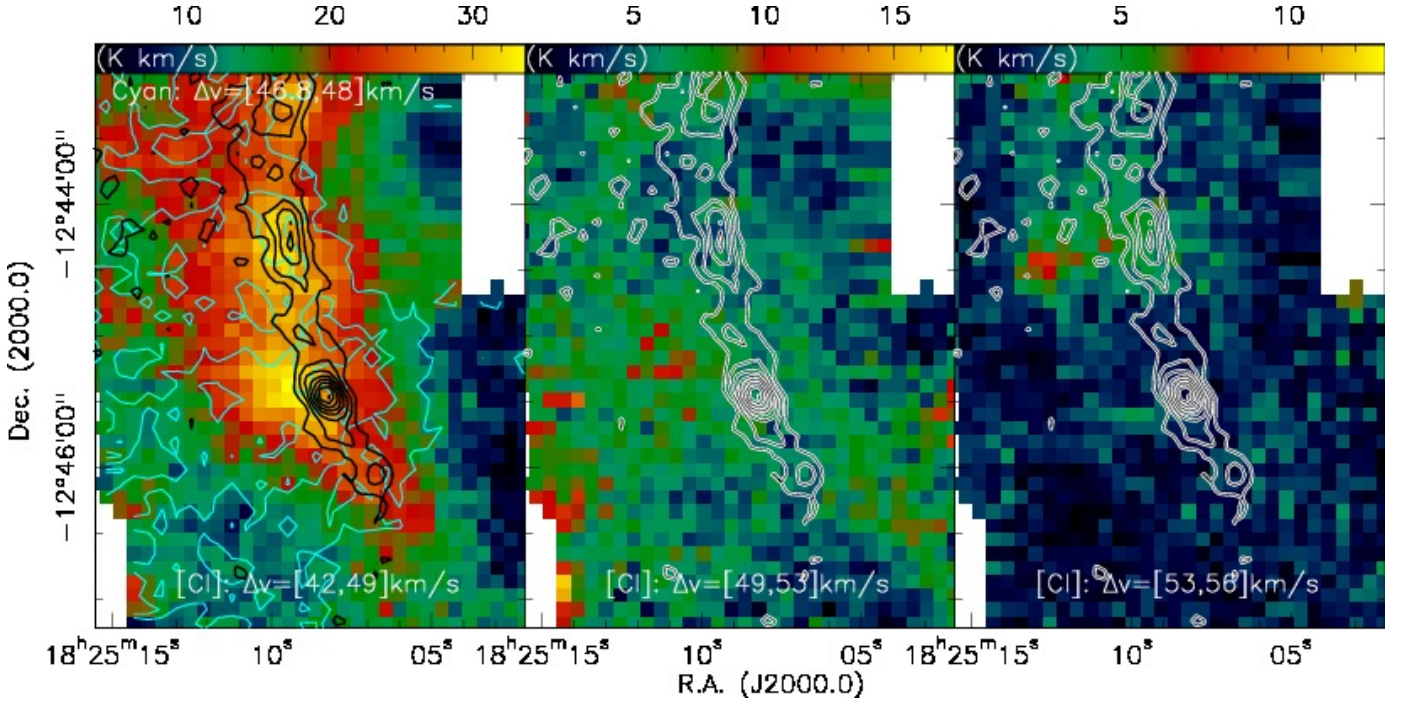


**Fig. 13.** IRDC18223: The color scale shows in the left, middle and right panel the emission from atomic carbon [CI] in the three velocity regimes marked above each panel. are [42;49], [43;49] and [43;55] km s<sup>-1</sup>. The cyan contours in the left panel correspond to [46.9;48.0] km s<sup>-1</sup>. The black contours always show the 1.2 mm continuum emission (Beuther et al., 2002) starting at 3 $\sigma$  level of 36 mJy beam<sup>-1</sup> and continuing in 3 $\sigma$  steps.

complex structure of the spectra, we do not report FWHM values for this region. Figure 15 presents emission of the two components integrated over a broad part of their spectra. In Beuther et al. (2012), it is argued that the two velocity components appear spatially interacting. In the new carbon data, this is best visible in the atomic phase where the 50 km s<sup>-1</sup> occupies the eastern part and the 100 km s<sup>-1</sup> mainly the western part of the observed region. In the ionized carbon [CII], the 50 km s<sup>-1</sup> emission is comparably very strong, however, the spatial separation of both components is less obvious. In contrast to that, the C<sup>18</sup>O(2–1) emission shows in general a similar structure as the atomic carbon [CI] with the main difference that the 50 km s<sup>-1</sup> appears less extended in the molecular gas. This is consistent with the observations of the other sources where we also saw a general tendency that the molecular C<sup>18</sup>O(2–1) emission is the most compact.

#### 4.2. Carbon phases versus hydrogen distributions

In order to quantitatively compare the distribution of the different carbon phases with the molecular gas of these regions, we constructed dust temperature and column density maps using the Herschel data obtained for the *Earliest Phases of Star Formation* key program (Ragan et al., 2012). We used PACS data at 100 and 160  $\mu$ m and SPIRE data at 250, 350 and 500  $\mu$ m. First all maps were convolved to the SPIRE 500  $\mu$ m resolution then mapped to identical grids. The spectral energy distribution (SED) at each pixel was fit employing the hierarchical Bayesian-fitting algorithm described in Kelly et al. (2012), which makes the assumption that the SED is well-fit by a modified Planck function as follows:

$$S_\nu = \Omega N \kappa_0 \left( \frac{\nu}{\nu_0} \right)^\beta B_\nu(T_d)$$

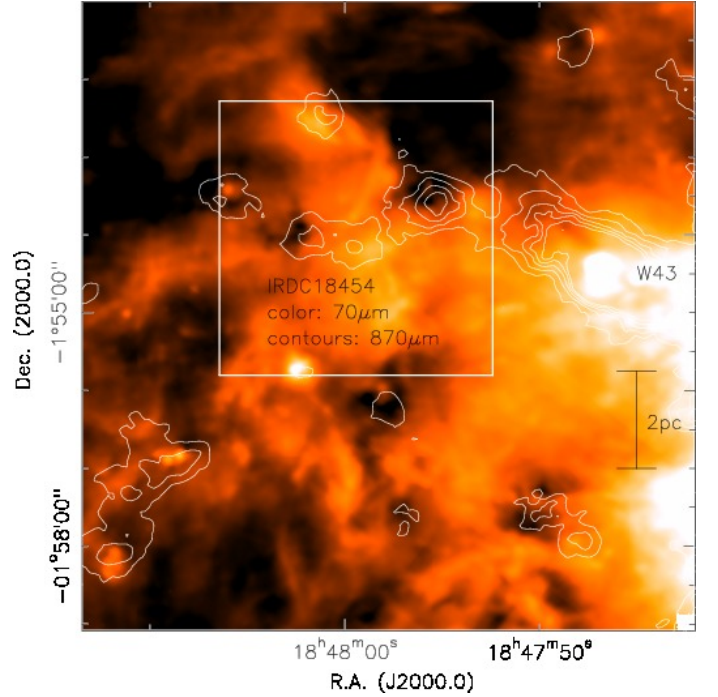


**Fig. 14.** IRDC 18454: Large-scale Herschel/PACS 70  $\mu$ m image of the IRDC 18223 region with 870  $\mu$ m ATLASGAL contours in steps of 0.4 mJy beam<sup>-1</sup>. The white box outlines the region of our carbon observations shown in Fig. 15.

where  $\Omega$  is the solid angle of the observation,  $N$  is the column density,  $B_\nu(T)$  is the Planck function, which is evaluated at the dust temperature,  $T_d$ , and  $\kappa_0(\nu/\nu_0)^\beta$  is the dust opacity. We assumed a  $\kappa_0$  of 0.006 cm<sup>2</sup> g<sup>-1</sup> at 1.3 mm wavelengths (Ossenkopf & Henning, 1994), which includes an assumed dust-to-gas ratio of 150 (Draine, 2011). The algorithm fits for  $N$ ,  $T_d$  and  $\beta$ . For

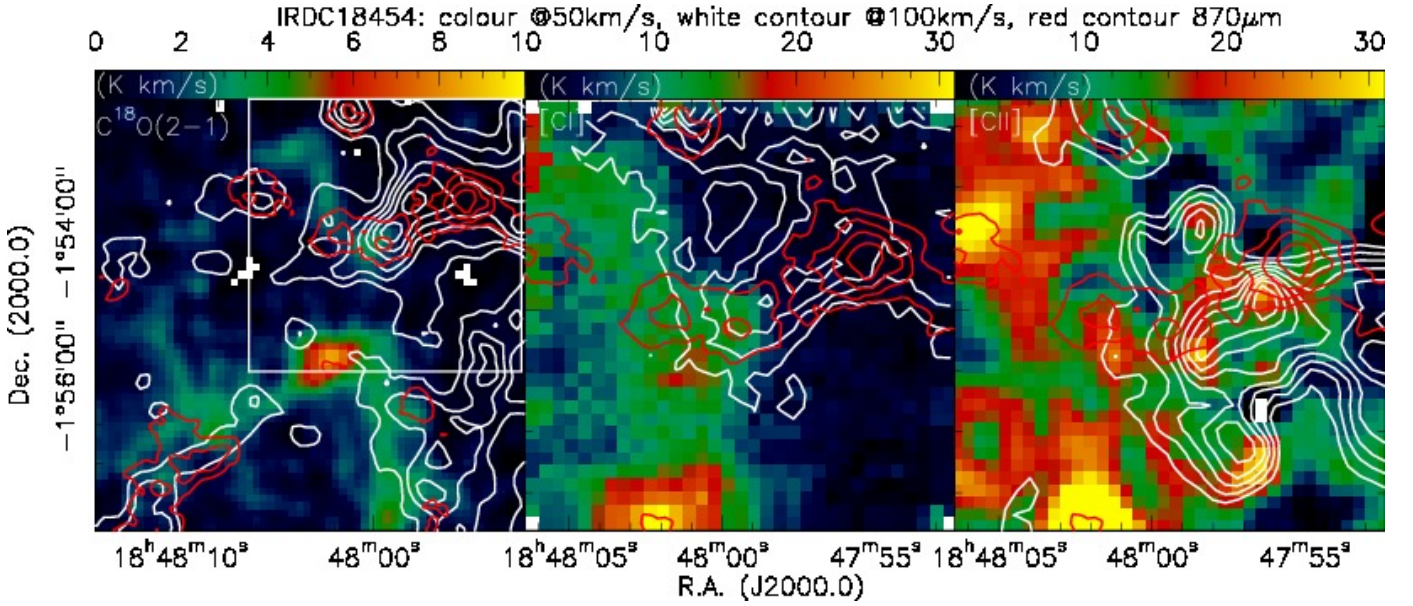


**Fig. 15.** IRDC18454: The color scale shows in the left, middle and right panel the emission from  $C^{18}O(2-1)$ ,  $[CI]$  and  $[CII]$ , respectively. The integration regimes for the three color images are  $[47;55] \text{ km s}^{-1}$ . The white contours in all three panels correspond to the emission from the same species only integrated from  $[80;120] \text{ km s}^{-1}$ . The red contours always show the ATLASGAL  $870 \mu\text{m}$  emission in levels of  $0.4 \text{ Jy beam}^{-1}$ .

the plots, we also show the equivalent  $A_V$  computed from the relation  $N_{H_2} = 0.95 \times 10^{21} \text{ cm}^{-2} (A_V / \text{mag})$ .

For the comparison, we used the integrated intensity maps of  $C^{18}O(2-1)$ ,  $[CI]$  and  $[CII]$  for the four regions with the velocity regimes presented in Figures 2, 7, 11 and 15. These images were smoothed to the spatial resolution of the SPIRE  $500 \mu\text{m}$  data of  $36.6''$ .

Figure 17 presents the scatter plots of the three gas phases with respect to the molecular ( $H_2$ ) column density, and one sees distinct differences between the molecular, neutral atomic and ionized atomic phases. The  $C^{18}O(2-1)$  emission strongly increases at low column densities, and then flattens off at column densities above  $10^{22} \text{ cm}^{-2}$ . The latter flattening can likely be attributed to freeze-out of the carbon monoxide at the low temperatures in these IRDCs (toward the cloud centers we find temperatures below  $20 \text{ K}$ , see for comparison, e.g., Kramer et al. 1999).

The atomic carbon also shows a correlation with the hydrogen column density, however, in general the relation is flatter and no clear break is visible. This confirms the previous morphological assessment that the atomic carbon is related to the dense molecular gas, however, weaker than the molecular  $C^{18}O$ . To compare our results with the recent cloud formation and  $[CI]$  emission models by Glover et al. (2014), we show as a dashed line in Fig. 17 the fit they conducted to their model data in their approximately linear regime below  $10 \text{ mag}$  extinction. The comparison with our data shows that below column densities of about  $10^{22} \text{ cm}^{-2}$  (or  $10 \text{ mag}$  extinction), the models and observations agree reasonably well. Toward higher column densities this linear relation between  $[CI]$  emission and molecular column density breaks down and the curves flatten. This is already indicated in the models by Glover et al. (2014), and even more prominent in our data since these observations go to higher column densities.

Finally, the ionized carbon emission exhibits almost no correlation with the general dense gas distribution. This confirms that ionized carbon is distributed in a much broader and widespread component than the molecular gas.

#### 4.3. Masses of carbon components

In addition to the morphologic analysis, we can use the spectral line data of the three different carbon phases to estimate the mass contributions of the ionized and atomic carbon as well as molecular CO to the gas phase carbon budget of the interstellar medium. For all three species, we calculate the corresponding column densities and masses assuming optically thin emission of the respective spectral lines.

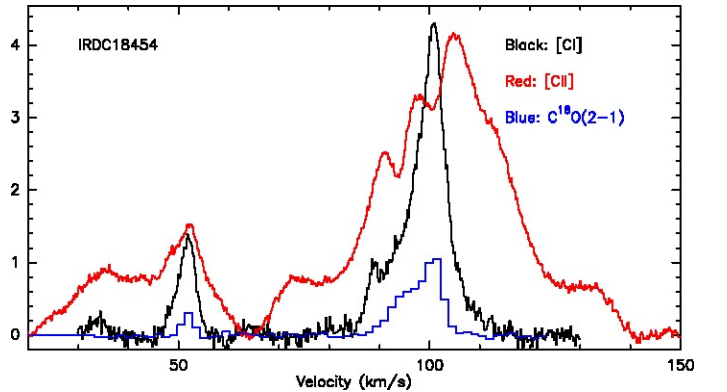


**Fig. 16.** IRDC18454:  $C^{18}O(2-1)$ ,  $[CI]$  and  $[CII]$  spectra (in K) averaged over the whole area of emission shown in Figure 15.

For the molecular  $C^{18}O$ , the column densities are calculated using classical expressions (e.g., Cabrit et al. 1988):

$$N_{C^{18}O} = \frac{6.97 \times 10^{15}}{\nu^2 \mu^2} T_{\text{ex}} e^{E_u/(kT_{\text{ex}})} \frac{\tau}{1 - e^{-\tau}} \int T_{\text{mb}} dv [\text{cm}^{-2}].$$

Here,  $\nu$ ,  $\mu$ ,  $T_{\text{ex}}$ ,  $E_u/k$ ,  $\tau$  and  $T_{\text{mb}}$  are the frequency, dipole moment ( $0.112 \text{ Debye}$ ), the excitation temperature, the upper energy level of  $15.8 \text{ K}$ , the optical depth and the main beam brightness temperature of the line, respectively. Assuming  $\tau \ll 1$  the term  $\frac{\tau}{1 - e^{-\tau}}$  approaches 1.



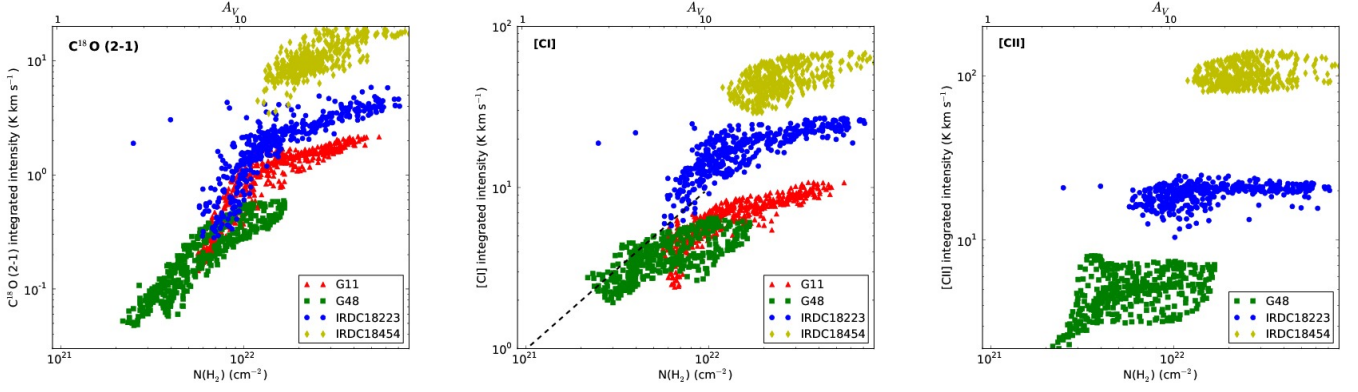


**Fig. 17.** Scatter plots of the integrated  $\text{C}^{18}\text{O}(2-1)$ , [CI] and [CII] emission versus the molecular column density and extinction (in mag) derived from the Herschel far-infrared data. The color-coding separates between the different regions as marked in each panel. The integration regimes are the same as those mentioned in the previous corresponding figures (for G48.66 only the main spectral component and for IRDC 18454 only the  $100 \text{ km s}^{-1}$  component are used). The dashed line in the middle panel shows the fit to the modeled [CI] data from Glover et al. (2014) who fitted their data in their approximately linear regime below 10 mag extinction. For IRDC 18454, we only use the  $100 \text{ km s}^{-1}$  component that is clearly associated with the W43 complex.

The atomic carbon [CI] column densities are calculated following Frerking et al. (1989):

$$N_{[\text{CI}]} = 5.94 \times 10^{15} \frac{1 + 3e^{-\frac{23.6}{T_{\text{ex}}}} + 5e^{-\frac{62.4}{T_{\text{ex}}}}}{3e^{-\frac{23.6}{T_{\text{ex}}}}} \int T_{\text{mb}} dv [\text{cm}^{-2}]$$

and for the ionized carbon [CII], the column densities are calculated following Goldsmith et al. (2012), eq. 26:

$$N_{[\text{CII}]} = 3.43 \times 10^{16} \left[ 1 + 0.5e^{91.25/T_{\text{kin}}} \left( 1 + \frac{2.4 \times 10^{-6}}{C_{ul}} \right) \right] \times \int T_{\text{mb}} dv [\text{cm}^{-2}]$$

with the kinetic gas temperature  $T_{\text{kin}}$  and the collision rate  $C_{ul} = R_{ul}n$  depending on the temperature, where  $R_{ul}$  is collision rate coefficient with  $\text{H}_2$  and  $n$  the density.

The remaining unknown in the equations above is the temperature of the gas. Since we are dealing with infrared dark clouds, hence the earliest evolutionary stages, for the molecular  $\text{C}^{18}\text{O}$  and the atomic [CI] we assume 15 K for all sources following multiple  $\text{NH}_3$  studies of IRDCs (e.g., Sridharan et al. 2005; Pillai et al. 2006; Dunham et al. 2011; Ragan et al. 2011; Wienen et al. 2012; Chira et al. 2013). Regarding the temperatures for the ionized carbon, this is less well determined. Langer et al. (2010) assume temperatures largely between 100 and 150 K for the diffuse ionized carbon, although above the level temperature of  $E_u/k$  of 91 K, the emissivity is basically constant, independent of the assumed excitation temperature. However, at least in G48.66 and IRDC 18454 we see a clear spatial correlation between the ionized carbon emission and that of the dense molecular CO. This indicates that the temperatures of the ionized carbon could be lower as well. To estimate the uncertainties based on the temperature, we calculated the masses of the ionized carbon for temperatures between 20 and 250 K at an average density  $n \sim 1 \times 10^3 \text{ cm}^{-3}$ . The corresponding collision rate coefficients with  $\text{H}_2$  are taken from the Leiden database for molecular spectroscopy (Schöier et al. 2005, <http://home.strw.leidenuniv.nl/moldata/>) where the para- and ortho rates are weighted following Le Boulrot (1991) and Gerlich (1990). While for IRDC 18454 in the vicinity of W43 collisions

with other partners than  $\text{H}_2$  may be possible as well, the good spatial correspondence of the [CII] with the molecular line data indicates that  $\text{H}_2$  should be the most dominant collisional partner. Figure 18 presents the corresponding results. For temperatures above 100 K, the corresponding masses do not vary significantly, however, going to lower temperatures, the values can vary by more than a factor of a few (see also Table 4).

To calculate the masses of the different carbon phases, we integrated the emission of the different spectral lines over the areas of their respective emission. For IRDC 18454, we only use the spectral component around  $100 \text{ km s}^{-1}$  since only that is unambiguously associated with the neighboring W43 complex. Table 4 presents the derived masses of the CO (converting  $\text{C}^{18}\text{O}$  to  $^{12}\text{CO}$  masses with a factor 500, Wilson & Rood 1994, applying the additional CO/ $\text{H}_2$  ratio of  $\sim 10^{-4}$  we have an estimate of the total gas mass), atomic and ionized carbon in our four target regions. We find that in all four regions, gas-phase carbon is most dominant in its molecular form, usually about 10 times more abundant than atomic carbon. Interestingly, the ratio between the ionized and the other two phases is less uniform. While ionized carbon is less abundant than atomic carbon in G11.11, we find more ionized than atomic carbon in the other three regions. One should keep in mind that these ratios depend on the covered areas since [CII] is usually found to be more extended than the other two phases. More details will be discussed in section 5.1.

#### 4.4. Estimates of bolometric luminosities and radiation fields

Further interesting parameters to characterize the emission of the different carbon phases is an evaluation of the bolometric luminosities in the regions as well as an estimation of the interstellar radiation field.

The bolometric luminosities are straightforward to estimate. We extract the total fluxes in our regions from the Herschel far-infrared data between 70 and  $500 \mu\text{m}$  (Ragan et al., 2012) and fit spectral energy distributions (SEDs) to the data points. The resulting SEDs give us estimates of the bolometric luminosities of the regions. Table 5 presents the bolometric luminosities  $L_{\text{bol}}$  derived this way ranging from a few thousand for G48.66 to more than  $10^5 L_{\odot}$  for IRDC 18454. These bolometric luminosities can partly be due to internal sources, but they are also produced by the external radiation penetrating and heating these clouds. To

**Table 4.** Masses of carbon phases

| phase                                                    | G11.11<br>(M <sub>⊙</sub> ) | G48.66<br>(M <sub>⊙</sub> ) | IRDC18223<br>(M <sub>⊙</sub> ) | IRDC18454 <sup>3</sup><br>(M <sub>⊙</sub> ) |
|----------------------------------------------------------|-----------------------------|-----------------------------|--------------------------------|---------------------------------------------|
| CO                                                       | 0.81                        | 0.30                        | 1.84                           | 13.4                                        |
| [CI]                                                     | 0.056                       | 0.025                       | 0.21                           | 1.6                                         |
| [CII]@50K                                                | < 0.012                     | 0.12 <sup>1</sup>           | 0.54                           | 14.8                                        |
| [CII]@100K                                               | < 0.005                     | 0.05 <sup>1</sup>           | 0.21                           | 5.7                                         |
| CO/[CI]/[CII]@50K                                        | 14.5/1/>0.2                 | 12/1/4.8                    | 8.8/1/2.6                      | 8.4/1/3.6 <sup>2</sup>                      |
| Approx. area of emission (pc <sup>2</sup> ) <sup>4</sup> | 5.2                         | 3.7                         | 6.5                            | 31.4                                        |

<sup>1</sup> The main component between 31 and 37 km s<sup>-1</sup>.<sup>2</sup> [CII] calculated at 100 K because of the energy input from the neighboring W43 region.<sup>3</sup> Only the 100 km s<sup>-1</sup> component is evaluated.<sup>4</sup> Based on the [CII] maps.

approximate the contribution of internal source luminosity to the total, we use the Ragan et al. (2012) catalog of point sources, which uses modified blackbody fits to the Herschel point source SED at 70, 100 and 160  $\mu$ m to compute the luminosities. We sum the luminosities of all point sources in the regions mapped in this work ( $L_{\text{point}}$ ) and tabulate them in Table 5. These values represent lower limits, as some point sources that were not detected at all PACS wavelengths are excluded from the Ragan et al. (2012) catalog, though we expect this additional contribution to be negligible. Nevertheless, it is clear that the point source luminosity contribution is on the order of a few percent of the total bolometric luminosity of the IRDCs. Thus, we conclude that  $L_{\text{bol}}$  is dominated by external irradiation. These bolometric luminosities may to first order appear large, in particular since we are studying infrared dark clouds. However, considering the large areas over which these bolometric luminosities are derived (between 9 and 31 pc<sup>2</sup>, Table 5), and taking into account that the dust emission is also due to external radiation, these values are plausible. We see a clear differentiation between the more isolated IRDCs G11.11, G48.66 and IRDC 18223 with bolometric luminosities in the  $10^4 L_{\odot}$  regime, and the very different IRDC 18454 that exceeds  $10^5 L_{\odot}$ . The latter high value is in agreement with IRDC 18454 being located in the direct environment of W43 with an estimated luminosity from the associated Wolf-Rayet cluster in excess of  $10^6 L_{\odot}$  (e.g., Blum et al. 1999; Beuther et al. 2012).

It is more difficult to estimate the interstellar radiation field. However, one can indirectly get an estimate of the interstellar radiation field from the dust temperature. Here, we follow the approach outlined in Glover & Clark (2012). Assuming that the dust is in thermal equilibrium, the main process responsible for heating the dust is the absorption of photons from the interstellar radiation field. Cooling is dominated by thermal emission from the dust, which for the dust properties assumed in their study (dust properties of non-coagulated grains coated with thick ice mantles) scales  $\propto T_d^6$ . In thermal equilibrium, one can then derive a relation between the interstellar radiation field  $G_0$  (here we use the Draine field which is 1.7 times the Habing field, e.g., Tielens 2005) and the dust temperature  $T_d^6$  as

$$G_0 = \frac{4.7 \times 10^{-31}}{5.6 \times 10^{-24}} \times \frac{1}{\chi(A_v)} \times T_d^6$$

where  $\chi(A_v)$  is an attenuation factor depending on the extinction. Glover & Clark (2012) evaluated  $\chi(A_v)$  for the above-mentioned dust model, and we use  $\chi(A_v) \sim 0.1$  corresponding to an average hydrogen column density  $N_H$  of  $\sim 10^{22} \text{ cm}^{-2}$ .

The median dust temperatures were again derived from the SED fits to the Herschel far-infrared data (Ragan et al., 2012) also used in section 4.2. The temperatures and corresponding  $G_0$  values are shown in Table 5. While the interstellar radiation field is on the order of a few 10 (in Draine units =  $2.7 \times 10^{-3} \text{ erg cm}^{-2} \text{ s}^{-1}$ ) for the three more quiescent IRDCs (G11.11, G48.66, IRDC18223), the estimated external radiation field exceeds 100 for IRDC 18454. The latter higher value is again no surprise since this region is in the direct neighborhood of the  $3.5 \times 10^6 L_{\odot}$  mini-starburst W43 (e.g., Beuther et al. 2012). As obvious in the above equation for  $G_0$ , the high sensitivity of the external radiation field on the dust temperature introduces considerable errors in these estimates. Since the four regions have four different temperatures, the values in Table 5 give also a rough estimate of the steep dependency of  $G_0$  on  $T_d$  and hence the uncertainties associated with this approach. Although just ball-park estimates, the luminosities and radiation fields derived this way are in rough agreement with each other. The large external radiation field and luminosity derived for IRDC 18454 also explain the much stronger emission of [CI] and [CII] in this complex.

**Table 5.** Luminosities and radiation fields

| Name       | $L_{\text{bol}}$<br>( $10^3 L_{\odot}$ ) | $L_{\text{point}}^a$<br>( $10^3 L_{\odot}$ ) | $T_d^b$<br>(K) | $G_0$<br>( $2.7 \times 10^{-3} \frac{\text{erg}}{\text{cm}^2 \text{ s}})^c$ | area<br>(pc <sup>2</sup> ) |
|------------|------------------------------------------|----------------------------------------------|----------------|-----------------------------------------------------------------------------|----------------------------|
| G11.11     | 12.5                                     | 0.02                                         | 20             | 54                                                                          | 11                         |
| G48.66     | 4.8                                      | 0.14                                         | 21             | 72                                                                          | 9                          |
| IRDC 18223 | 21.5                                     | 0.76                                         | 18             | 29                                                                          | 13                         |
| IRDC 18454 | 194                                      | 2.27                                         | 23             | 124                                                                         | 31                         |

<sup>a</sup> Luminosities of the point sources identified within our fields by Ragan et al. (2012).<sup>b</sup> Median dust temperatures.<sup>c</sup> These are commonly referred to as “Draine units” (1.7 times the Habing field).

## 5. Discussion

### 5.1. Carbon phases

As expected, the C<sup>18</sup>O(2–1) emission traces the dense gas observable in the dust continuum emission very well. Similarly the [CI] emission is a reasonable proxy of the dense gas (see also Glover et al. 2014), however, it appears somewhat more widespread on average. The [CII] emission shows a less uniform picture and varies from a non-detection (G11.11) to com-



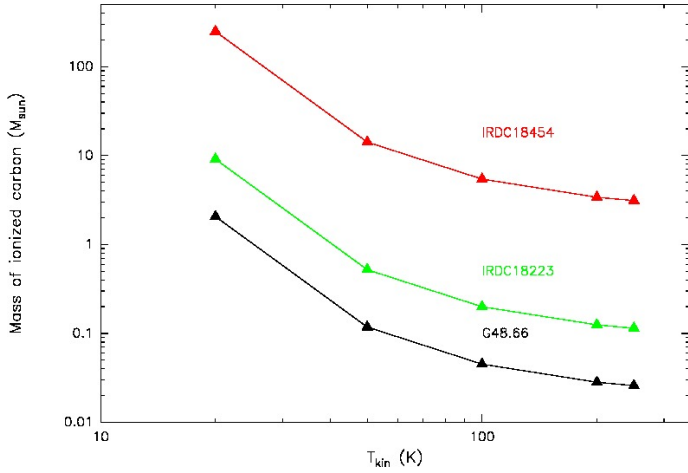


**Fig. 18.** Masses of ionized carbon in the three regions where the line is clearly detected. We calculated the masses assuming different temperatures at an average density of  $10^3 \text{ cm}^{-3}$  as outlined in section 4.3.

pact sources (G48.66 and IRDC 18454) as well as more diffuse components (G48.66, IRDC 18223, IRDC 18454). These differences are particularly prominent in the scatter plots in Figure 17.

Ratios between atomic carbon and CO for typical molecular clouds have usually been reported in the 20% to 30% regime (e.g., Frerking et al. 1989; Beuther et al. 2000), and Tauber et al. (1995) infer a lower limit of 17% for the Orion Bar photon dominated region (PDR). In contrast to that, the largest ratio of atomic carbon to CO we find is  $\sim 12\%$  in IRDC 18454 whereas the ratio is lower in the other regions going down to values of  $\sim 7\%$  in the most quiescent region G11.11 (§2). A similar value of 8% was also found in the lower-spatial-resolution [CII]/ $^{13}\text{CO}$  study of the G48.66 region by Ossenkopf et al. (2011). Although our sample of four regions is too small to derive firm conclusions, we do see a trend of increasing atomic-to-molecular gas ratio from the earliest, most quiescent infrared dark and starless clouds to regions that are in a more evolved environments with radiation sources nearby, e.g., the high-mass protostellar object IRAS 18223-1243 at the northern end of the IRDC 18223 or the W43 mini-starburst near IRDC 18454.

Regarding the ionized carbon, the situation is less conclusive. While we do not detect [CII] emission in our most quiescent region G11.11, it is strongly detected in the other regions with higher ionized than atomic carbon gas abundances. Since the temperatures are more uncertain for the ionized carbon, the ratios are also less well determined. For example the ionized-to-atomic gas ratio may vary between 4 and 9.3 for IRDC 18454 depending on the assumed temperature for the ionized carbon of 50 or 100 K, respectively. The highest ionized carbon abundances are again seen in the region IRDC 18454 that is exposed to the intense radiation field of the W43 mini-starburst.

The Herschel GOTC<sup>+</sup> survey has revealed that a significant fraction of molecular  $\text{H}_2$  gas is not traced by CO but this sometimes dubbed “dark gas” may be traced by the [CII] emission (Langer et al., 2010; Velusamy et al., 2010; Pineda et al., 2010, 2013). While the ratio of CO-dark  $\text{H}_2$  gas depends on the density, Pineda et al. (2013) estimate for the whole GOTC<sup>+</sup> survey that approximately 28% of the  $\text{H}_2$  gas can be missed by the CO emission, but these values can go even above 50% for the more diffuse lower extinction parts of the clouds (Velusamy et al., 2010). Although deriving CO-dark gas fractions is not the scope of our paper, we do see wherever we detect [CII] emission that

it is spatially significantly more extended than the dense  $\text{C}^{18}\text{O}$  and dust continuum emission, consistent with the GOTC<sup>+</sup> results. While the  $\text{C}^{18}\text{O}$  emission traces the dense gas associated with the star-forming regions, in particular the [CII] emission traces the environment and is much more sensitive to the external UV field. For [CII] emission associated with molecular clouds, Pineda et al. (2010) find that in many cases low far-UV fields and densities in the regime  $10^{3.5} - 10^{5.5} \text{ cm}^{-3}$  reproduce the data well, but they also find exception where strong far-UV fields and higher densities are required. While the latter situation resembles the IRDC 18454 complex, the former lower far-UV fields rather resemble the other three target regions of our mini-survey.

Extended [CII] emission is also regularly observed from strong PDRs, a recent prominent example being M17SW (Pérez-Beaupuits et al., 2012). They find that the [CII] emission on the one hand traces parts of the PDR that are not found by other tracers, and that on the other hand the [CII] emission is seen from deep in the cloud. The latter is interpreted as additional evidence of the clumpy nature of the dense ISM. In contrast to M17SW, we are dealing largely with much lower far-UV fields, however, again the IRDC 18454 region partly resembles the extended emission [CII] emission as well as the association with the dense gas and hence the clumpiness of star-forming regions.

## 5.2. Gas flows

Since the different carbon phases trace different parts of the forming and evolving clouds, the [CII], [CI] and  $\text{C}^{18}\text{O}$  lines should harbor signatures of the cloud formation history or external UV illumination. In the framework of converging gas flows, kinematic signatures may be embedded in the more diffuse gas components (e.g., Vázquez-Semadeni et al. 2006; Heitsch et al. 2008; Glover & Clark 2012; Clark et al. 2012), and we investigate such potential signatures in our datasets.

For G11.11 and IRDC 18454 this turns out to be more difficult. While in the former source [CII] remains undetected and hence we do not have much information about the more diffuse parts of the cloud, it is interesting that we find a line width increase in the  $\text{C}^{18}\text{O}$  and [CI] emission close to a position of multiple  $\text{N}_2\text{H}^+$  spectral features in high-resolution PdBI data (Ragan et al. in prep.). Such an enhanced line width or multiple peaks can be interpreted as signatures of global collapse of high-mass star-forming regions (e.g., Smith et al. 2013). In comparison to that, in the IRDC 18454 region the [CII] emission is very strong and shows the multiple velocity components (§4.1.4). These multiple velocity components have already previously been reported in molecular and ionized gas emission (Anderson et al., 2011; Beuther et al., 2012), and the controversy stands whether these two velocity components at 50 and  $100 \text{ km s}^{-1}$  are signs of cloud-cloud interaction at the galactic-bar/inner-spiral-arm interface or whether they are simply chance alignments along the line of sight (Nguyen Luong et al., 2011; Beuther et al., 2012). This ambiguity may be resolved in the future when accurate parallax distances from maser sources at both velocities become available through the Bessel survey (Brunthaler et al., 2011).

Investigating the other two regions, promising kinematic signatures can be found. For G48.66, in particular the [CII] emission turns out to be interesting. Although the averaged FWHM line width of the main gas component in the molecular, atomic and ionized gas does not exhibit large spreads between 1.7 and  $3.3 \text{ km s}^{-1}$ , the additional high-velocity gas component visible in Fig. 8 is spatially clearly offset to the north from the main component around the  $v_{\text{lsr}}$  (Fig. 7). Looking at the velocity structure, the first moment map in Fig. 9 exhibits a strong velocity gradi-

ent from north to south directly across the main infrared dark gas filament and site of active star formation. This steep velocity gradient at the location of the IRDC indicates a large velocity shear and by that enhanced Rayleigh-Taylor instability. Therefore, we suggest that the IRDC may at least partly be formed through that instability. Attempts to produce observational predictions of colliding flow signatures have focused mainly on CO transitions (e.g., Heitsch et al. 2008; Clark et al. 2012), but the diverse morphologies and dynamics that we observe in the [CII] line, such as the velocity gradients and correlations with other tracers described above, give us a promising avenue to potentially discern between various cloud assembly processes.

The other infrared dark filament IRDC 18223 does also show different velocity components, but the kinematic signatures are different. Comparing only the averaged spectral signatures, the ionized and atomic carbon as well as  $C^{18}O$  appear similar with multiple velocity components (Fig. 12). However, spatially the ionized carbon is distinct from the atomic and molecular phase, and it is largely found in a diffuse distribution at the edge of the cloud. In contrast to that, the multiple velocity components of the atomic carbon and  $C^{18}O$  exhibit clear spatial substructures and appear relatively similar between both phases (Figures 11 and 13). The main spectral component around the  $v_{lsr}$  of  $\sim 45.5 \text{ km s}^{-1}$  is clearly associated with the dense filament traced by the dust continuum emission. But even within that main component, the more red-shifted part between  $46.8$  and  $48 \text{ km s}^{-1}$  is already offset from the filament to the south-east (Figures 11 and 13). Going to higher velocities, the second spectral component between  $49$  and  $54 \text{ km s}^{-1}$  is more diffusely distributed (Fig. 13, middle panel), whereas at even higher velocities between  $53$  and  $56 \text{ km s}^{-1}$ , we find again a compact gas component east of the filament (Fig. 13) right panel). As mentioned in section 4.1.3, the spectrum in Fig. 12 shows an additional blue-shifted [CI] component, however, that is only found at the lowest edge of the mapped region and we cannot give more details about that. With blue- and red-shifted gas in diffuse as well as compact components found around the main dense gas filament, we again tentatively interpret these spectral and spatial structures as evidence that the main filament of active star formation has formed out of a kinematically active gas stream that likely converged in the region of the filament.

## 6. Conclusions

With the aim of studying the different carbon gas phases (ionized, atomic and molecular) during the early high-mass star formation stages, we observed four infrared dark clouds at high spatial resolution in the spectral emission lines of ionized ([CII]) and atomic ([CI]) carbon as well as molecular carbon monoxide ( $C^{18}O(2-1)$ ) with Herschel, SOFIA, APEX and the IRAM 30 m telescopes. Except for the ionized [CII] line in one region, we could map all gas components toward all four target regions.

- While as expected the molecular gas is always closely associated with the dense gas filaments visible in infrared extinction as well as dust emission, the atomic carbon often has a similar appearance. It also traces the dense gas, however, the atomic gas distribution appears a bit more extended than the  $C^{18}O$  maps. The averaged line widths within the different regions are slightly smaller for the  $C^{18}O(2-1)$  line compared to the atomic [CI] emission.
- In contrast to that, the ionized carbon [CII] emission exhibits a larger spread in morphologies over the different regions. While it remains undetected in the most quiescent region, it

shows strong emission toward the IRDC in the environment of the W43 starburst. Furthermore, the spatial structure of the ionized carbon varies between rather diffuse emission at the cloud edges to structures that are clearly associated with the dense gas.

- The data allow us to estimate the relative abundances of the different carbon phases within these IRDCs. The ratio between atomic carbon and molecular CO mass ranges between  $7$  and  $12\%$ , lower than values found in other molecular clouds, with the lowest values found in the most quiescent environment. Although with only four regions, the statistical basis is still poor, the data indicate that the ratio of atomic to molecular gas depends on the evolutionary stage of the region as well as the radiation field the regions are exposed to. In the three regions where [CII] is detected, its abundances is always higher by a factor of a few than that of [CI].
- Similar to that, also the ionized carbon is most strongly detected in the environment of the W43 mini-starburst. However, for the dark clouds the signatures vary significantly. While [CII] remains undetected toward the most quiescent region G11.11, it is easily and strongly detected toward the G48.66 IRDC that is not much more evolved and that also does not have strong radiation sources in the environment. Hence, the [CII] emission does not only depend on external radiation sources but other factors must be important as well.
- While still in a very young evolutionary stage, G48.66 exhibits the strongest kinematic signatures of gas flows in the [CII] emission. This indicates that kinematically active regions can exhibit stronger [CII] emission as well. Although model predictions about kinematic signatures of converging gas flows are scarce or non-existent, we interpret the strong [CII] velocity gradient across the G48.66 dark filament as suggestive evidence for filament formation within kinematically very active gas flows.
- For the IRDC 18223, we see multiple red- and blue-shifted velocity components. While the spatial structure of the ionized carbon in this region is relatively diffuse, the atomic and molecular gas exhibits spatially distinct cloud components in the environment of the dense filament. Again, we interpret this complex spatial and spectral substructures as tentative evidence for gas flows that may form the active star formation sites at converging points. In addition to this, in IRDC 18223 we find enhanced [CII] emission in the direction of two bipolar outflow lobes. While not conclusive yet, it may indicate that [CII] emission can also be caused by the kinematic activity of jets and outflows.

In summary, mapping star-forming regions at comparable spatial scales in the ionized, atomic and molecular phases allows us to constrain the carbon budget as well as the gas kinematics in great detail. Since cloud and star formation takes place in diverse environments, often one line does not tell the same story for different regions, hence, mapping all the different gas phases together is an important mean to understand the cloud and star formation processes in a global sense. While this study targeted mainly IRDCs, it will be important to extend similar studies to more evolved evolutionary stages.

While maps of molecular and atomic gas can be obtained with ground-based facilities well, Herschel mainly did single-pointing studies of the ionized carbon, and not many spectral line maps were obtained with that space observatory. SOFIA has now proven as a very efficient observatory to map clouds in the



[CII] and other far-infrared spectral lines, and we hope to get many more exciting data from this observatory in the future.

*Acknowledgements.* We would like to thank Rahul Shetty for helping to implement the dust temperature fitting algorithm. We also thank the anonymous referee as well as the editor Malcolm Walmsley for insightful comments improving the paper. SER acknowledges support from grant RA 2158/1-1 which is part of the DFG-SPP 1573 ‘The Physics of the Interstellar Medium’.

## References

- Anderson, L. D., Bania, T. M., Balser, D. S., & Rood, R. T. 2011, *ApJS*, 194, 32
- Bergin, E. A., Hartmann, L. W., Raymond, J. C., & Ballesteros-Paredes, J. 2004, *ApJ*, 612, 921
- Beuther, H., Henning, T., Linz, H., et al. 2010, *A&A*, 518, L78
- Beuther, H., Kramer, C., Deiss, B., & Stutzki, J. 2000, *A&A*, 362, 1109
- Beuther, H., Linz, H., Tackenberg, J., et al. 2013, *A&A*, 553, A115
- Beuther, H., Schilke, P., Menten, K. M., et al. 2002, *ApJ*, 566, 945
- Beuther, H. & Sridharan, T. K. 2007, *ApJ*, 668, 348
- Beuther, H. & Steinacker, J. 2007, *ApJ*, 656, L85
- Beuther, H., Tackenberg, J., Linz, H., et al. 2012, *A&A*, 538, A11
- Blum, R. D., Damineli, A., & Conti, P. S. 1999, *AJ*, 117, 1392
- Brunthaler, A., Reid, M. J., Menten, K. M., et al. 2011, *Astronomische Nachrichten*, 332, 461
- Cabrit, S., Goldsmith, P. F., & Snell, R. L. 1988, *ApJ*, 334, 196
- Carlhoff, P., Nguyen Luong, Q., Schilke, P., et al. 2013, *A&A*, 560, A24
- Chira, R.-A., Beuther, H., Linz, H., et al. 2013, *A&A*, 552, A40
- Clark, P. C., Glover, S. C. O., Klessen, R. S., & Bonnell, I. A. 2012, *MNRAS*, 424, 2599
- Cubick, M., Stutzki, J., Ossenkopf, V., Kramer, C., & Röllig, M. 2008, *A&A*, 488, 623
- Cyganowski, C. J., Whitney, B. A., Holden, E., et al. 2008, *AJ*, 136, 2391
- de Graauw, T., Helmich, F. P., Phillips, T. G., et al. 2010, *A&A*, 518, L6
- Draine, B. T. 2011, *Physics of the Interstellar and Intergalactic Medium* (Princeton Series in Astrophysics)
- Dunham, M. K., Rosolowsky, E., Evans, II, N. J., Cyganowski, C., & Urquhart, J. S. 2011, *ApJ*, 741, 110
- Fallscheer, C., Beuther, H., Zhang, Q., Keto, E., & Sridharan, T. K. 2009, *A&A*, 504, 127
- Frerking, M. A., Keene, J., Blake, G. A., & Phillips, T. G. 1989, *ApJ*, 344, 311
- Garay, G., Faúndez, S., Mardones, D., et al. 2004, *ApJ*, 610, 313
- Gerlich, D. 1990, *J. Chem. Phys.*, 92, 2377
- Glover, S. C. O. & Clark, P. C. 2012, *MNRAS*, 421, 116
- Glover, S. C. O., Clark, P. C., Micic, M., & Molina, F. 2014, *ArXiv e-prints*, 1403.3530
- Glover, S. C. O., Federrath, C., Mac Low, M., & Klessen, R. S. 2010, *MNRAS*, 404, 2
- Glover, S. C. O. & Mac Low, M.-M. 2011, *MNRAS*, 412, 337
- Goldsmith, P. F., Langer, W. D., Pineda, J. L., & Velusamy, T. 2012, *ApJS*, 203, 13
- Heitsch, F., Hartmann, L. W., Slyz, A. D., Devriendt, J. E. G., & Burkert, A. 2008, *ApJ*, 674, 316
- Henning, T., Linz, H., Krause, O., et al. 2010, *A&A*, 518, L95
- Henning, T. & Salama, F. 1998, *Science*, 282, 2204
- Herrmann, F., Madden, S. C., Nikola, T., et al. 1997, *ApJ*, 481, 343
- Heyminck, S., Graf, U. U., Güsten, R., et al. 2012, *A&A*, 542, L1
- Kainulainen, J., Ragan, S. E., Henning, T., & Stutz, A. 2013, *A&A*, 557, A120
- Kelly, B. C., Shetty, R., Stutz, A. M., et al. 2012, *ApJ*, 752, 55
- Köster, B., Störzer, H., Stutzki, J., & Sternberg, A. 1994, *A&A*, 284, 545
- Kramer, C., Alves, J., Lada, C. J., et al. 1999, *A&A*, 342, 257
- Kramer, C., Jakob, H., Mookerjee, B., et al. 2004, *A&A*, 424, 887
- Kuiper, R., Klahr, H., Beuther, H., & Henning, T. 2010, *ApJ*, 722, 1556
- Langer, W. D., Velusamy, T., Pineda, J. L., et al. 2010, *A&A*, 521, L17
- Larson, R. B. 1981, *MNRAS*, 194, 809
- Le Boulton, J. 1991, *A&A*, 242, 235
- Nguyen Luong, Q., Motte, F., Schuller, F., et al. 2011, *A&A*, 529, A41
- Ormel, C. W., Shipman, R. F., Ossenkopf, V., & Helmich, F. P. 2005, *A&A*, 439, 613
- Ossenkopf, V. & Henning, T. 1994, *A&A*, 291, 943
- Ossenkopf, V., Ormel, C. W., Simon, R., Sun, K., & Stutzki, J. 2011, *A&A*, 525, A9+
- Pérez-Beaupuits, J. P., Wiesemeyer, H., Ossenkopf, V., et al. 2012, *A&A*, 542, L13
- Pilbratt, G. L., Riedinger, J. R., Passvogel, T., et al. 2010, *A&A*, 518, L1
- Pillai, T., Wyrowski, F., Menten, K. M., & Krügel, E. 2006, *A&A*, 447, 929
- Pineda, J. L., Langer, W. D., Velusamy, T., & Goldsmith, P. F. 2013, *A&A*, 554, A103
- Pineda, J. L., Velusamy, T., Langer, W. D., et al. 2010, *A&A*, 521, L19
- Pitann, J., Linz, H., Ragan, S., et al. 2013, *ApJ*, 766, 68
- Ragan, S., Henning, T., Krause, O., et al. 2012, *A&A*, 547, A49
- Ragan, S. E., Bergin, E. A., & Wilner, D. 2011, *ApJ*, 736, 163
- Ragan, S. E., Henning, T., Tackenberg, J., et al. 2014, *A&A*, 568, A73
- Rathborne, J. M., Jackson, J. M., & Simon, R. 2006, *ApJ*, 641, 389
- Roelfsema, P. R., Helmich, F. P., Teyssier, D., et al. 2012, *A&A*, 537, A17
- Röllig, M., Ossenkopf, V., Jeyakumar, S., Stutzki, J., & Sternberg, A. 2006, *A&A*, 451, 917
- Sato, M., Reid, M. J., Brunthaler, A., & Menten, K. M. 2010, *ApJ*, 720, 1055
- Schöier, F. L., van der Tak, F. F. S., van Dishoeck, E. F., & Black, J. H. 2005, *A&A*, 432, 369
- Schuller, F., Menten, K. M., Contreras, Y., et al. 2009, *A&A*, 504, 415
- Shetty, R., Glover, S. C., Dullemond, C. P., & Klessen, R. S. 2011, *MNRAS*, 412, 1686
- Smith, R. J., Shetty, R., Beuther, H., Klessen, R. S., & Bonnell, I. A. 2013, *ApJ*, 771, 24
- Sridharan, T. K., Beuther, H., Saito, M., Wyrowski, F., & Schilke, P. 2005, *ApJ*, 634, L57
- Stahler, S. W. & Palla, F. 2005, *The Formation of Stars* (ISBN 3-527-40559-3. Wiley-VCH)
- Stutzki, J., Stacey, G. J., Genzel, R., et al. 1988, *ApJ*, 332, 379
- Tackenberg, J., Beuther, H., Plume, R., et al. 2013, *A&A*, 550, A116
- Tauber, J. A., Lis, D. C., Keene, J., Schilke, P., & Buettgenbach, T. H. 1995, *A&A*, 297, 567
- Tielens, A. G. G. M. 2005, *The Physics and Chemistry of the Interstellar Medium* (Cambridge University Press)
- Tielens, A. G. G. M. & Hollenbach, D. 1985, *ApJ*, 291, 722
- van der Wiel, M. H. D. & Shipman, R. F. 2008, *A&A*, 490, 655
- Vázquez-Semadeni, E., Ryu, D., Passot, T., González, R. F., & Gazol, A. 2006, *ApJ*, 643, 245
- Velusamy, T., Langer, W. D., Pineda, J. L., et al. 2010, *A&A*, 521, L18
- Wang, K., Zhang, Q., Testi, L., et al. 2014, *MNRAS*, 439, 3275
- Wienen, M., Wyrowski, F., Schuller, F., et al. 2012, *A&A*, 544, A146
- Wilson, T. L. & Rood, R. 1994, *ARA&A*, 32, 191
- Young, E. T., Becklin, E. E., Marcum, P. M., et al. 2012, *ApJ*, 749, L17
- Zhang, B., Moscadelli, L., Sato, M., et al. 2014, *ApJ*, 781, 89